J. Fluid Mech. (1986), *vol.* 165, *pp.* 79–130
Printed in Great Britain

Numerical study and physical analysis of the pressure and velocity fields in the near wake of a circular cylinder

By M. BRAZA, P. CHASSAING AND H. HA MINH
Institut de Mécanique des Fluides, Laboratoire associé au C.N.R.S.,
2 rue Camichel, 31071 Toulouse Cedex, France

(Received 3 August 1984 and in revised form 13 October 1985)

The dynamic characteristics of the pressure and velocity fields of the unsteady incompressible laminar wake behind a circular cylinder are investigated numerically and analysed physically. The governing equations, written in a velocity–pressure formulation and in conservative form, are solved by a predictor–corrector pressure method, a finite-volume second-order-accurate scheme and an alternating-direction-implicit (ADI) procedure. The initiation mechanism for vortex shedding and the evaluation of the unsteady body forces are presented for Reynolds-number values of 100, 200 and 1000.

The vortex shedding is generated by a physical perturbation imposed numerically for a short time. The flow transition becomes periodic after a transient time interval. The frequency of the drag and lift oscillations agree well with the experimental data.

The study of the interactions of the unsteady pressure and velocity fields shows the phase relations between the pressure and velocity, and the influence of different factors: the strongly rotational viscous region, the convection of the eddies and the almost inviscid flow.

The interactions among the different scales of structures in the near wake are also studied, and in particular the time-dependent evolution of the secondary eddies in relation to the fully developed primary ones is analysed.

1. Introduction

The unsteady viscous flow behind a circular cylinder has been the object of numerous experimental and numerical studies, especially from the fluid mechanics and hydraulics engineering points of view, because of the fundamental mechanisms that his flow exhibits and its numerous industrial applications. The majority of these applications concern the unsteady features of the wake rather than the unsteady dynamic characteristics near the wall.

Thus, most of the experimental studies investigate the unsteady behaviour of the alternating vortices in the wake. The work of Tessié-Solier (1931), Camichel (1931) and Crausse (1936) should be mentioned, as well as the more recent studies of Kovasznay (1949), Roshko (1954), Berger (1964), Davies (1976), Tritton (1971) and Cantwell (1975), among others. The above works investigate the more global character of the dynamics of the flow, covering in some cases study of the domain of laminar transition to turbulence.

This flow configuration can also be considered as a very convenient test case for fluid-dynamics computations, which explains why a lot of numerical works have been

devoted to this type of flow. The first simulation of the vortex paths by Kármán (1911) is based upon an inviscid approach. More recent simulations of the two-dimensional unsteady Navier–Stokes equations for this flow are developed in the work of Son & Hanratty (1969), Jain & Rao (1969), Thoman & Szewczyk (1969), Jordan & Fromm (1972), Lin, Pepper & Lee (1976), Daube & Ta Phuoc Loc (1978), Martinez (1979) and Ha Minh, Boisson & Martinez (1980).

Finally the unsteady flow past a circular cylinder has been studied by discrete eddy simulations, by Chorin (1973) and Spalart, Leonard & Baganoff (1983), among others.

All the above numerical studies, except the last one, provide results in the range of Reynolds numbers 40–1000. These methods have the following common characteristics: they solve the unsteady Navier–Stokes equations in two-dimensional Helmholtz (vorticity–stream function) formulation; they describe the relevant flow by global parameters such as Strouhal number as a main feature of the unsteady wake, drag and lift coefficients in the wall region; nevertheless, poor analysis is provided for the near-wake characteristics. The main goals of the present study are consequently to (i) clarify some physical aspects of the initiation of vortex shedding; (ii) analyse the interactions of the velocity and pressure fields outside and inside the wake and study the interactions of the near-wake pressure field with the distant one; and (iii) analyse the different types of structures that develop as the Reynolds number increases.

The numerical simulation is based upon a finite-volume velocity–pressure formulation of the unsteady Navier–Stokes equations. A semi-implicit second-order-accurate scheme is employed. Although the present paper concentrates on the physical aspects of the unsteady flow around a circular cylinder, it also shows, through the analysis of the results, the many potentialities and advantages of a pressure–velocity numerical code applied even in non-confined (external) flows. Hence, the outlines of the numerical procedure are presented in §3, following the theoretical formulation of the problem in §2. The discussion of the results in the light of the above main points is the object of §4. Most of the results concern the unsteady flow past the circular cylinder, for Reynolds numbers of 100, 200 and 1000.

2. The theoretical formulation

2.1. *The equations*

The governing equations for the unsteady flow of an incompressible viscous fluid past a circular cylinder are the classical continuity and Navier–Stokes equations. They are written in a logarithmic–polar coordinate system, sketched in figure 1(*a*), where

$$\tilde{x} = \theta, \quad \tilde{u} = V_\theta, \tag{1}$$

$$\tilde{y} = \ln r, \quad \tilde{v} = V_r. \tag{2}$$

The following dimensionless variables are used:

$$x = \tilde{x}, \quad y = \frac{\tilde{y}}{a}, \quad t = \frac{\tilde{t}U}{a}, \quad P = \frac{\tilde{P}}{\rho U_\infty^2}, \quad u = \frac{\tilde{u}}{U_\infty}, \quad v = \frac{\tilde{v}}{U_\infty}, \quad Re = \frac{2U_\infty a}{\nu}, \tag{3}$$

with a the radius of the cylinder, ν the kinematic viscosity and U_∞ the upstream velocity.

The continuity equation and the convection and diffusion terms of the momentum

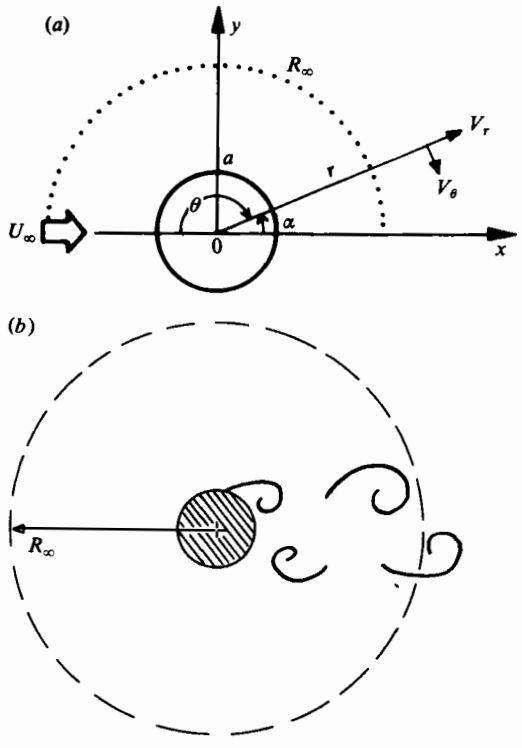

FIGURE 1. (*a*) Flow configuration and coordinate system. (*b*) The boundary conditions on the external radius.

equations are written in conservative form with respect to the above dimensionless variables:

$$\operatorname{div} \boldsymbol{V} = 0, \tag{4}$$

$$\frac{\partial u}{\partial t} + \operatorname{div}(\boldsymbol{V}u) - \frac{2}{Re}\operatorname{div}(\operatorname{grad} u) = -\frac{1}{e^y}\frac{\partial P}{\partial x} + S_u, \tag{5}$$

$$\frac{\partial v}{\partial t} + \operatorname{div}(\boldsymbol{V}v) - \frac{2}{Re}\operatorname{div}(\operatorname{grad} v) = -\frac{1}{e^y}\frac{\partial P}{\partial y} + S_v, \tag{6}$$

where

$$S_u = -\frac{uv}{e^y} - \frac{2}{Re}\frac{1}{e^{2y}}\left(u - 2\frac{\partial v}{\partial x}\right), \tag{7}$$

$$S_v = \frac{u^2}{e^y} - \frac{2}{Re}\frac{1}{e^{2y}}\left(v + 2\frac{\partial u}{\partial x}\right). \tag{8}$$

2.2. *The boundary conditions*

The wall boundary conditions are those of impermeability and non-slip:

$$u = 0, \quad v = 0. \tag{9}$$

In the physical domain the flow is not confined. Nevertheless, a fictitious external circular boundary is needed at a large distance R_∞ from the cylinder (figure 1*b*) in order to solve numerically (4)–(8). The corresponding boundary conditions are chosen so as to minimize the blockage effect due to this frontier.

Equations (5) and (6) are written at infinity by using the following assumptions:

$$\frac{\partial u}{\partial t} \to 0 \quad \text{for } v \to \infty; \tag{10a}$$

$$\frac{\partial P}{\partial x} \to P_\infty \quad \text{for } v \to \infty; \tag{10b}$$

the convective velocity vector V of the dimensionless term div (Vu) is that of the uniform flow:

$$u = -(\sin x)\, U_\infty \quad \text{and} \quad v = (\cos x)\, U_\infty. \tag{10c}$$

Equation (5) can be written as follows:

$$\frac{\partial^2 u}{\partial x^2} + \frac{\partial^2 u}{\partial y^2} = e^y \frac{Re}{2}\left(\cos x \frac{\partial u}{\partial y} - \sin x \frac{\partial u}{\partial x}\right) + \sin x - e^y \frac{Re}{2} \cos x \sin x. \tag{11}$$

An analogous equation can be obtained for the v-component. The flow at infinity is hence governed by Oseen's linearized equations in the same way as reported by Dennis & Chang (1970) for the vorticity equation.

Equation (11) can then be solved analytically, the homogeneous equation corresponding to (11) being

$$\frac{\partial^2 u}{\partial x^2} + \frac{\partial^2 u}{\partial y^2} = e^y \frac{Re}{2}\left(\cos x \frac{\partial u}{\partial y} - \sin x \frac{\partial u}{\partial x}\right). \tag{12a}$$

It has an analytic solution

$$Uh(x, y) = e^{K \cos x} \sum_{i=0}^{\infty} A_i F_i(K) \cos(ix), \tag{12b}$$

where

$$K(y) = \tfrac{1}{4} e^y Re, \tag{12c}$$

F_i is a second-kind Bessel function and A_i a sequence of constants.

It can be shown that there exists a function $G(x)$ such that the solution $Uh(x, y)$ can be written as:

$$Uh(x, y) = G(x) \exp(K(\cos x - 1) - 0.5y). \tag{13}$$

The general solution of (12b) is the sum of $Uh(x, y)$ and of one particular solution of (11).

It is easy to show that the function

$$Up(x, y) = -\sin x \tag{14a}$$

verifies (11).

The solution of this equation is then

$$u(x, y) = G(x) \exp(K(\cos x - 1) - 0.5y) + Up(x, y). \tag{14b}$$

Hence

$$u(x, y) - Up(x, y) = G(x) \exp(K(\cos x - 1) - 0.5y). \tag{14c}$$

The above relation is written for two values of y: $y_\infty = \ln(R_\infty)$ and $y_{\infty-1} = y_\infty - \Delta y$ where Δy is the mesh spacing. Hence,

$$\frac{u(x, y_\infty) - Up(x, y_\infty)}{u(x, y_{\infty-1}) - Up(x, y_{\infty-1})} = H(x, y_\infty, y_{\infty-1}), \tag{15}$$

where $$H(x, y_\infty, y_{\infty-1}) = \frac{\exp(K_\infty(\cos x - 1) - 0.5y_\infty)}{\exp(K_{\infty-1}(\cos x - 1) - 0.5y_{\infty-1})}.$$

A relation similar to (15) can be obtained for the v-component, by setting $Vp(x, y) = \cos x$. Hence, the boundary conditions for u and v at infinity are given by

$$u(x, y_\infty) = u(x, y_{\infty-1})\, H(x, y_\infty, y_{\infty-1}) + (1 - H)\sin x, \tag{16a}$$

$$v(x, y_\infty) = v(x, y_{\infty-1})\, H(x, y_\infty, y_{\infty-1}) - (1 - H)\cos x. \tag{16b}$$

It can be shown that function $H(x, y, t)$ vanishes for points of the external radius outside the wake. It tends to unity for points of the external radius in the wake region. Hence,

$$V(x, y)_{y=y_\infty} \to U_\infty \quad \text{outside the wake,} \tag{17}$$

$$\left(\frac{\partial V}{\partial y}\right)_{y=y_\infty} \to 0 \quad \text{in the wake region.} \tag{18}$$

The boundary conditions at infinity, obtained in this way, take into account two different features of the flow of a viscous fluid around the cylinder: the strongly irrotational and convective flow upstream; and the boundary-layer type of flow in the wake.

The above Oseen solution allows the progressive and smooth change from Dirichlet to Neumann kinds of boundary conditions. Hence, the boundary conditions at infinity are those of uniform flow outside the wake and those of zero derivatives in the y-direction for points in the wake.

3. The numerical study

The method used is based upon a predictor–corrector pressure scheme first proposed by Chorin (1968) and Amsden & Harlow (1970) (the simplified marker and cell, SMAC method). A staggered grid for the velocity and pressure is used, as developed by Harlow & Welch (1965) in the marker and cell, MAC method. In addition, we suggest in this paper a contribution to a rigorous calculation of the pressure in relation to a semi-implicit solution of the time-dependent equations. Only an outline of the numerical method is presented in the following: a detailed development can be found in the work of Braza (1981).

3.1. *The principle of the numerical method*

As the values of the velocity and pressure are known at the time step n, an approximate pressure field, $P^* = P^n$, is substituted into the momentum equations (5) and (6). These are then solved for a corresponding velocity field V^*. The vector form of the corresponding momentum equation is

$$\frac{V^* - V^n}{\Delta t} + \operatorname{div}(V^n V^*) - \operatorname{div}(\operatorname{grad} V^*) = -\operatorname{grad} P^* + S_v, \tag{19a}$$

whereas the exact momentum equation at time step $(n+1)$ is

$$\frac{V^{n-1} V^n}{\Delta t} + \operatorname{div}(V^n V^{n+1}) - \operatorname{div}(\operatorname{grad} V^{n+1}) = -\operatorname{grad} P^{n+1} + S_v. \tag{19b}$$

The intermediate velocity V^* carries the exact vorticity but it does not necessarily satisfy the mass conservation (4) like the true velocity at time step $(n+1)$, V^{n+1}.

Since both fields V^* and V^{n+1} carry the same vorticity even on the boundaries, they can be related by an auxiliary potential function ϕ, such that

$$V^{n+1} = V^* - \operatorname{grad}\phi. \tag{20}$$

The potential ϕ is calculated by taking the divergence of (20) and assuming that $\operatorname{div}(V^{n+1}) = 0$. A Poisson equation for ϕ is then obtained:

$$\nabla^2\phi = \operatorname{div} V^*. \tag{21}$$

The true velocity at time step $(n+1)$ can now be evaluated from (20). The corresponding pressure is then deduced by combining the exact momentum equation at time step $n+1$ (19a), the approximate one (19) and (20):

$$\operatorname{grad} P^{n+1} = \operatorname{grad}\left(P^n + \frac{\phi}{\Delta t}\right) + \operatorname{div}(V^n \operatorname{grad}\phi) - \nu\nabla^2(\operatorname{grad}\phi). \tag{22}$$

Whenever the momentum equation is approximated by a fully explicit scheme, as in the case of the SMAC method, the pressure equation is reduced to the simpler one

$$P^{n+1} = P^n + \frac{\phi}{\Delta t}. \tag{23}$$

The viscous term $\nu\nabla^2(\operatorname{grad}\phi)$ is maintained in some implicit numerical methods (Lilley 1976; Cazalbou 1983), but the convective term is often neglected. Nevertheless, this term could be important in high-Reynolds-number calculations, whereas the influence of the viscous term is very weak. In the present method, both the exact equation (22) and the approximate one (23) are used for the $Re = 1000$ case. The results are similar for both cases, but the convergence is improved when using the completed equation (22). The boundary conditions for the pressure correction are deduced from (20) written at the boundary.

It is noteworthy that (21)–(23) are only valid for interior mesh points. The direct use of the above relations for boundary points of the grid would require special treatment. This calculation is not necessary for the present numerical method, where staggered grids for velocity and pressure are used and integration is performed over elementary control volumes. Whenever pressure values on boundaries are necessary, they are deduced directly from the momentum and continuity equations written at the boundary.

3.2. *Finite-volume approximations for the governing equations*

The governing equations are integrated over elementary control volumes defined in figure 2. It is well known that this technique enhances the local mass and momentum conservation near the boundaries better than a simple finite-difference approximation scheme (see, for example, Ta Phuoc Loc 1980). The numerical schemes used in the following are second-order accurate only. Consequently, a very refined grid is needed for moderate- and high-Reynolds-number calculations.

The momentum equations

Equations (5) and (6) are integrated over the corresponding control volumes for the u- and v-components (figures 2b, c). The integrals of the divergence terms over each control volume are transformed to boundary integrals using the Gauss divergence

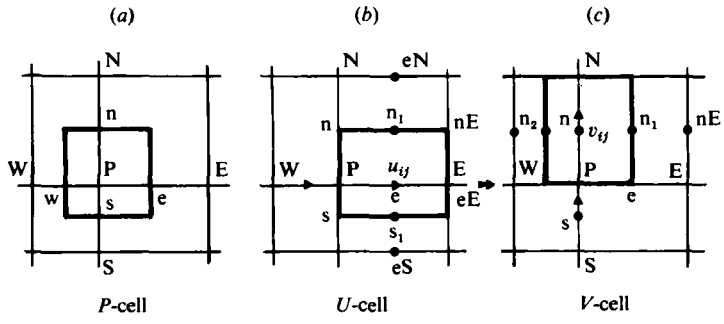

FIGURE 2. The elementary control volumes: (*a*) *P*-cell; (*b*) *U*-cell; (*c*) *V*-cell.

theorem. Hence, the u-equation is written

$$\iint_{\Omega_u} \frac{\partial u^*}{\partial t}\,\mathrm{d}w + \int_{\Gamma_u} V^n \eta u^*\,\mathrm{d}w - \int_{\Gamma_u} \nu\,\mathrm{grad}\,u^*\,\eta\,\mathrm{d}w = -\iint_{\Omega_u} \frac{1}{\rho\,\mathrm{e}^y}\frac{\partial P^n}{\partial x}\,\mathrm{d}w + \iint_{\Omega_u} S_u\,\mathrm{d}w, \tag{24}$$

with η the exterior unit vector normal to the elementary volume contour Γ_u.

Assuming that the terms u^*, $\partial P^n/\partial x$, S_u are constant over Ω_u and that V has a constant value over each side of the Γ_u contour, (24) is written

$$\begin{aligned}
&\frac{\partial u^*}{\partial t}\,\Omega_u + u^*_{\mathrm{E}}\,u_{\mathrm{E}}\,A_{\mathrm{vE}} - u^*_{\mathrm{P}}\,u_{\mathrm{P}}\,A_{\mathrm{vP}} + u^*_{\mathrm{n}_1}\,v_{\mathrm{n}_1}\,A_{\mathrm{hn}_1} - u^*_{\mathrm{s}_1}\,v_{\mathrm{s}_1}\,A_{\mathrm{hs}_1} \\
&\quad - \nu\left[\frac{1}{\exp(y_{\mathrm{E}})}\left(\frac{\partial u^*}{\partial x}\right)_{\mathrm{E}} A_{\mathrm{vE}} - \frac{1}{\exp(y_{\mathrm{P}})}\left(\frac{\partial u^*}{\partial x}\right)_{\mathrm{P}} A_{\mathrm{vP}}\right. \\
&\quad \left. + \frac{1}{\exp(y_{\mathrm{n}_1})}\left(\frac{\partial u^*}{\partial y}\right)_{\mathrm{n}_1} A_{\mathrm{hn}_1} - \frac{1}{\exp(y_{\mathrm{s}_1})}\left(\frac{\partial u^*}{\partial y}\right)_{\mathrm{s}_1} A_{\mathrm{hs}_1}\right] \\
&\qquad = -\frac{1}{\exp(y_{\mathrm{e}})}\left(\frac{\partial P^*}{\partial x}\right)_{\mathrm{e}} \Omega_u + S_u\,\Omega_u.
\end{aligned} \tag{25}$$

A_{vE}, A_{vP}, A_{hn_1} and A_{hs_1} stand for the vertical and horizontal sides of the u-cell. Because of the logarithmic-polar coordinates, these lengths have the following expressions (cf. figure 2).

$$A_{\mathrm{vE}} = \exp(y_{\mathrm{E}})\,(y_{\mathrm{nE}} - y_{\mathrm{sE}}); \quad A_{\mathrm{vP}} = \exp(y_{\mathrm{P}})\,(y_{\mathrm{n}} - y_{\mathrm{s}}), \tag{26}$$

$$A_{\mathrm{hn}_1} = \exp(y_{\mathrm{n}_1})\,(x_{\mathrm{nE}} - x_{\mathrm{n}}); \quad A_{\mathrm{hs}_1} = \exp(y_{\mathrm{s}_1})\,(x_{\mathrm{sE}} - x_{\mathrm{s}}). \tag{27}$$

The points E and P do not belong to the u^* grid system; hence the velocities u^*_{E} and u^*_{P} are calculated from the u^*_{w}, u^*_{e} and u^*_{eE} ones, by using linear second-order-accurate interpolations. The spatial derivatives in (25) are approximated by centred-finite-difference schemes.

The nonlinear convection term is artificially linearized after splitting it into two parts. The first is the vector V, assumed to be a convection vehicle, taken at the time step n. The second is the velocity component u^*, a transportable property of the fluid and taken at time step $(n+1)$. A Peaceman–Rachford (1955) alternating-direction-implicit (ADI) method is used for the temporal approximations in (25). The temporal derivative for each ADI step is approximated by forward-time relations.

Equation (25) is written for the two ADI steps as follows:

First ADI step

$$\frac{(u^*)^{n+\frac{1}{2}}-u^n}{\frac{1}{2}(\Delta t)}\Omega_u+(u^*)_{\mathrm{E}}^{n+\frac{1}{2}}u_{\mathrm{E}}^n A_{v\mathrm{E}}-(u^*)_{\mathrm{P}}^{n+\frac{1}{2}}u_{\mathrm{P}}^n A_{v\mathrm{P}}+(u^*)_{\mathrm{n}_1}^n v_{\mathrm{n}_1}^n A_{\mathrm{hn}_1}-(u^*)_{\mathrm{s}_1}^n v_{\mathrm{s}_1}^n A_{\mathrm{hs}_1}$$
$$-\nu\left[\frac{1}{\exp(y_{\mathrm{E}})}\left(\frac{\partial u^*}{\partial x}\right)_{\mathrm{E}}^{n+\frac{1}{2}}A_{v\mathrm{E}}-\frac{1}{\exp(y_{\mathrm{P}})}\left(\frac{\partial u}{\partial x}\right)_{\mathrm{P}}^{n+\frac{1}{2}}A_{v\mathrm{P}}\right.$$
$$\left.+\frac{1}{\exp(y_{\mathrm{n}_1})}\left(\frac{\partial u}{\partial y}\right)_{\mathrm{n}_1}^{n}A_{\mathrm{hn}_1}-\frac{1}{\exp(y_{\mathrm{s}_1})}\left(\frac{\partial u}{\partial y}\right)_{\mathrm{s}_1}^{n}A_{\mathrm{hs}_1}\right]$$
$$=-\frac{1}{\exp(y_{\mathrm{e}})}\left(\frac{\partial P^n}{\partial x}\right)_{\mathrm{e}}\Omega_u+S_u\Omega_u. \quad (28)$$

Second ADI step

$$\frac{(u^*)^{n+1}-(u^*)^{n+\frac{1}{2}}}{\frac{1}{2}(\Delta t)}\Omega_u+(u^*)_{\mathrm{E}}^{n+\frac{1}{2}}u_{\mathrm{E}}^n A_{v\mathrm{E}}-(u^*)_{\mathrm{P}}^{n+\frac{1}{2}}u_{\mathrm{P}}^n A_{v\mathrm{P}}+(u^*)_{\mathrm{n}_1}^{n+1}v_{\mathrm{n}_1}^n A_{\mathrm{hn}_1}$$
$$-(u^*)_{\mathrm{s}_1}^{n+1}v_{\mathrm{s}_1}^n A_{\mathrm{hs}_1}-\nu\left[\frac{1}{\exp(y_{\mathrm{E}})}\left(\frac{\partial u^*}{\partial x}\right)_{\mathrm{E}}^{n+\frac{1}{2}}A_{v\mathrm{E}}-\frac{1}{\exp(y_{\mathrm{P}})}\left(\frac{\partial u}{\partial x}\right)_{\mathrm{P}}^{n+\frac{1}{2}}A_{v\mathrm{P}}\right.$$
$$\left.+\frac{1}{\exp(y_{\mathrm{n}_1})}\left(\frac{\partial u^*}{\partial y}\right)_{\mathrm{n}_1}^{n+1}A_{\mathrm{hn}_1}-\frac{1}{\exp(y_{\mathrm{s}_1})}\left(\frac{\partial u^*}{\partial y}\right)_{\mathrm{s}_1}^{n+1}A_{\mathrm{hs}_1}\right]$$
$$=-\frac{1}{\exp(y_{\mathrm{e}})}\left(\frac{\partial P^*}{\partial x}\right)_{\mathrm{e}}\Omega_u+S_u\Omega_u. \quad (29)$$

Equations (28) and (29) are written for all the nodes of the unknown u^*, leading to a set of tridiagonal linear systems. These are solved by the fast-Choleski–Gauss method.

The boundary conditions for the approximate velocity field u^* are of similar nature to those for the true velocity at time step $n+1$. Hence the approximate velocity u vanishes at the wall and it is calculated by the Oseen solution (cf. (16a) and (16b)), written in terms of u^* for the external boundary.

The solution of the v transport equation is achieved in the same way as for the u-component one.

The Poisson equation for the pressure correction

For the Poisson equation a fictitious temporal term is introduced in (21) to allow an ADI iterative method. This equation then becomes

$$\frac{\partial\phi}{\partial\tau}=\operatorname{div}(\operatorname{grad}\phi)-\operatorname{div}V^*, \quad (30)$$

which is integrated over the P control volume Ω_P and transformed according to the same assumptions as for the u-component equation.

Within each physical time step n, after calculating the approximate velocity field V^*, the Poisson equation (30) is solved for a number of iterations sufficient to achieve convergence. An iterative ADI scheme is used. To this end, the fictitious time step $\Delta\tau$ is split into two parts: $(k, k+\frac{1}{2})$ and $(k+\frac{1}{2}, k+1)$. The index k designates the range of the iteration and is not related to the physical time index n. Convergence is

obtained when the relative error between the two last values of ϕ is less than a given threshold value.

The boundary conditions for ϕ are deduced from (20), written in the normal direction for each boundary. Hence, on the wall

$$\frac{\partial \phi}{\partial y} = 0, \tag{31}$$

and for the external boundary

$$e^{y_\infty - y_{\infty-1}} \left(\frac{\partial \phi}{\partial y}\right)_{y=y_{\infty-1}} H = \left(\frac{\partial \phi}{\partial y}\right)_{y=y_\infty}, \tag{32}$$

where H is the Oseen function given by (15).

The choice of the fictitious time step $\Delta\tau$ is made either empirically or by a Wachspress (1964) optimization but the number of iterations does not significantly vary between the two methods. The optimization is not found to be very successful for this problem, as all the boundary conditions for ϕ are not of the Dirichlet type.

3.3. *Accuracy*

The accuracy of the present method has been evaluated by solving a test problem for which an analytical solution is available as a function of time and Reynolds number. The Taylor problem was used (see Batchelor 1960), the solution of which is given by the following equations:

$$u = -\cos x \sin y \, e^{-2t/Re}; \tag{33}$$

$$v = \sin x \cos y \, e^{-2t/Re}; \tag{34}$$

$$P = -0.25 (\cos 2x + \cos 2y) \, e^{-4t/Re}. \tag{35}$$

The Navier–Stokes equations are solved numerically by the present method in a square domain of dimensions $(\frac{1}{2}\pi, \frac{1}{2}\pi)$. The evolution of the error as a function of the time step Δt, the mesh space Δx and the Reynolds number is given in figures 3(a, b, c) respectively.

The temporal accuracy is found to be almost of second order. Actually the second-order temporal accuracy of an ADI method has been shown theoretically by Douglas (1955), only for the solution of the diffusion equation. As the present problem involves a particular temporal approximation for the nonlinear convection terms, the order of accuracy is found to be slightly smaller than two. This is clearly seen from the slopes of the error evolution in figure 3(a).

The space accuracy is found to be of second order, as shown in figure 3(b). The error as a function of the Reynolds number remains bounded and small up to $Re = 10000$ (figure 3c).

3.4. *The values of the parameters*

The numerical parameters $\Delta x, \Delta y, \Delta t$, as well as the number of nodes necessary for the simulation of the flow past the circular cylinder, are evaluated in order to ensure the stability and to minimize the numerical error for each value of the Reynolds number. Different values for the mesh spacing, time step and external radius are tested. The set of parameters finally chosen for computation, at each value of Reynolds number, are those giving results as close as possible to experimental ones. The value of the external radius is selected as the minimum one which gives a velocity and pressure field being almost insensitive to a longer distance. In particular, for

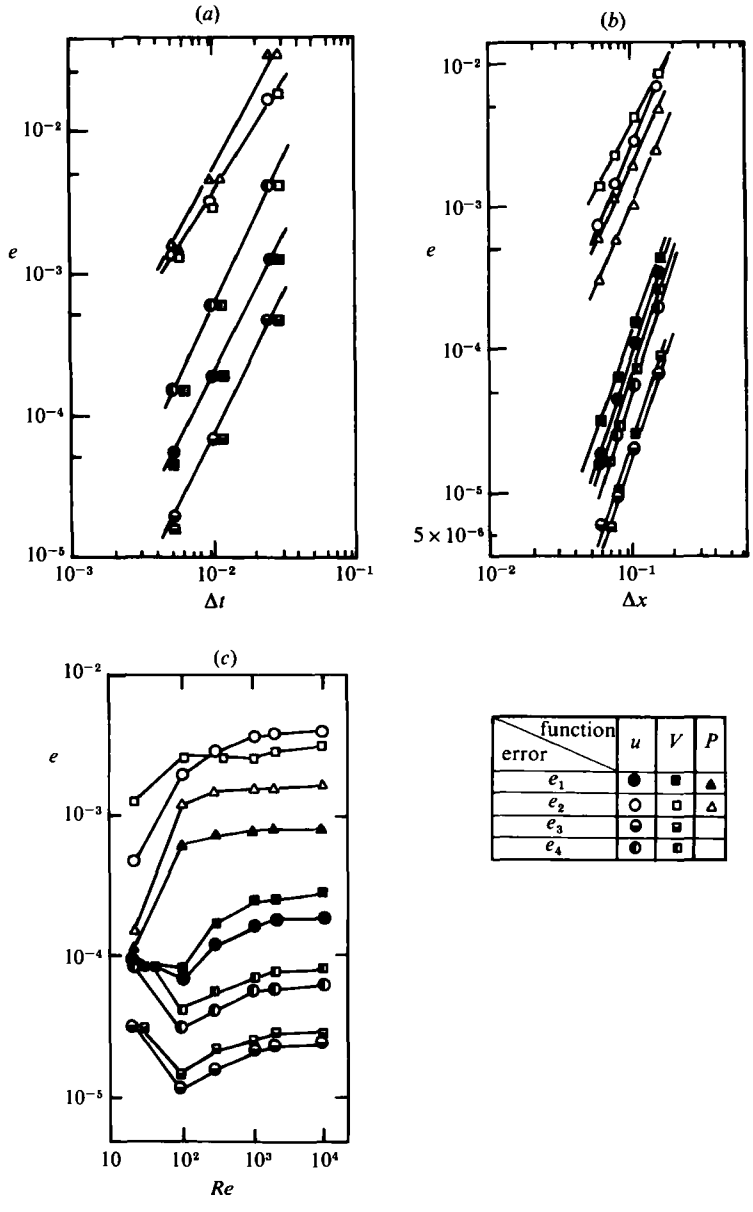

FIGURE 3. (*a*) Test problem: the error as a function of Δt; $Re = 1.0$, $\Delta x = 0.079$, $t = 0.6$. (*b*) Test problem: the error as a function of Δx; $Re = 60$, $t = 0.44$. (*c*) The error as function of Reynolds number; $\Delta t = 0.010$, $\Delta x = 0.079$, $t = 0.5$. $e_1 = \max(|F_{ij} - f_{ij}|)$; $e_2 = e_1/|F_{ij}|$; $e_3 = (1/N_x N_y)\Sigma|F_{ij} - f_{ij}|$; $e_4 = \Sigma|F_{ij} - f_{ij}|/\Sigma F_{ij}$; where F is the analytic solution, f the numerical value and N_x and N_y respective the number of nodes in the x- and y-directions.

$Re = 1000$, two different sets of parameters are tested, both giving results close to experimental ones (figures 9). The parameters finally chosen and the CPU time are given in table 1. Most of the computations are done on IBM 3033 computer. For the $Re = 1000$, case (*b*), the computation has been carried out on a CRAY 1S computer of the Centre de Calcul Vectoriel pour la Recherche of France.

Reynolds number	$\Delta x \Delta y$	External radius	Number of unknowns	Time step	Total physical time	CPU (s) per time step
20	$\frac{1}{32}\pi \frac{1}{32}\pi$	135.46	10608	0.01	22	1.664†
40	$\frac{1}{32}\pi \frac{1}{32}\pi$	135.46	10608	0.025	30	1.664†
100	$\frac{1}{40}\pi \frac{1}{40}\pi$	114.55	13530	0.02	100	2.69†
200	$\frac{1}{40}\pi \frac{1}{40}\pi$	114.55	13530	0.02	100	2.69†
Case (*a*)						
1000	$\frac{1}{50}\pi \frac{1}{50}\pi$	114.12	18360	0.02	100	5.84†
Case (*b*)						
1000	$\frac{1}{60}\pi \frac{1}{60}\pi$	114.12	31476	0.01	100	2.10‡

† I.B.M. 3033, Centre National Universitaire Sud de Calcul (CNUSC).
‡ CRAY-1S, Centre de Calcul Vectoriel pour la Recherche (CCVR).

TABLE 1. The values of the numerical parameters

4. The results

The results of the steady flow for Reynolds numbers 20 and 40 are reported first to allow comparison with experimental data and with other numerical results. Hence, the efficiency of the method for solving a non-confined flow and for predicting accurately the pressure distribution is established. The results of the unsteady flow for the Reynolds numbers 100, 200 and 1000 are then presented. Third, the unsteady behaviour of secondary eddies developing in the flow at $Re = 1000$, as well as their interactions with the main eddies by two-dimensional mechanisms, are analysed.

In the following, the conventional coefficients of the lift and drag on the cylinder are

$$C_L = \frac{\text{lift force}}{0.5\rho U_\infty^2 2a}, \quad C_D = \frac{\text{drag force}}{0.5\rho U_\infty^2 2a}; \tag{36}$$

$$C_{LP} = \int_0^{2\pi} P_w \sin x \, dx, \quad C_{LV} = \frac{2}{Re}\int_0^{2\pi} \omega_w \cos x \, dx; \tag{37}$$

$$C_{DP} = \int_0^{2\pi} P_w \cos x \, dx, \quad C_{DV} = \frac{2}{Re}\int_0^{2\pi} \omega_w \sin x \, dx; \tag{38}$$

where the subscripts P and V respectively represent the contributions of the pressure and viscous forces. P_w is the dimensionless wall pressure and ω_w is the dimensionless wall vorticity defined as $\omega_w = \omega a / U_\infty$.

The dimensionless frequency of vortex shedding is the Strouhal number $St = fD/U_\infty$, where f is the frequency, D the diameter of the cylinder and U_∞ the uniform-flow velocity. The pressure coefficient is defined as: $C_P = 2(P - P_\infty)/\rho U_\infty^2$.

4.1. *The steady flow*

For Reynolds numbers of 20 and 40 the flow reaches a steady state at about $t = 7$ and $t = 15$ respectively. Two attached vortices are formed behind the cylinder. The time evolution of the reattachment length and the velocity field of the steady state reached are shown in figures 4(*a*. *b*). Good agreement with the experimental results of Coutanceau & Bouard (1977*a*, *b*) is obtained. Agreement is also good with numerical results of Martinez (1979), using a vorticity–stream function formulation.

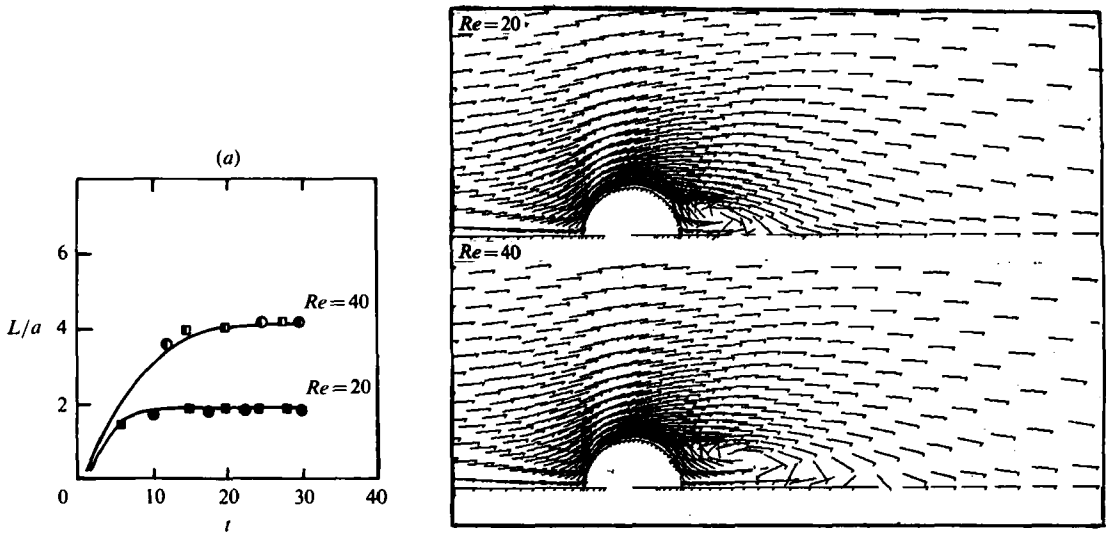

FIGURE 4. (a) Reattachment length: ——, this study; ■ ◧, Coutanceau & Bouard (1977a, b); ● ◐, Martinez (1979). (b) Velocity fields.

In figure 5(a) the distribution of the wall vorticity is shown. Comparison with the numerical results of Martinez (1979) and Fornberg (1980) is found to be satisfactory. Figure 5(b) shows the distribution of the wall pressure compared with the experimental results of Grove *et al.* (1964) for $Re = 20$ and 40. The pressure coefficient C_P shown in this figure is defined as $C_P = (P - P_0 + \frac{1}{2}\rho U_\infty^2)/(\frac{1}{2}\rho U_\infty^2)$, with P_0 the front stagnation-point pressure. The calculation of the wall pressure by the present method agrees well with these experimental data.

The drag coefficient and the separation angle as a function of Reynolds number compared with other experimental and numerical results are shown in figures 6(a, b). Good agreement is again obtained.

The computation of the flow at $Re = 1000$ shows that the steady state is also reached but after a longer transition time (figure 7). The oscillations of the drag coefficient, before symmetry has been achieved, are due to the oscillations of the reattachment point forward and backward. This computation is carried out without imposing any perturbation on the field.

Experimental results for the flow at a Reynolds number greater than 40 report a loss of symmetry in the wake. As the Reynolds number increases alternating eddies are formed and convected in the wake. Hence, the above computation apparently does not represent a physically real case. The reason for this is given in §4.2.

4.2. *Vortex shedding*

As the Reynolds number becomes higher than 40 not every destabilization of the flow, random or not, can be damped and this leads to an asymmetrical eddy pattern. This generates the alternating separation of the vortices, which are convected and diffused away from the cylinder, forming the well-known Kármán vortex paths. Such destabilizing effects always occur during any physical experiment on the flow around a circular cylinder. Conceptually, the origin of the destruction of the symmetric pattern can be explained by the presence of multiple perturbation sources in the physical model: non-uniform inlet conditions; irregularity of the boundary conditions

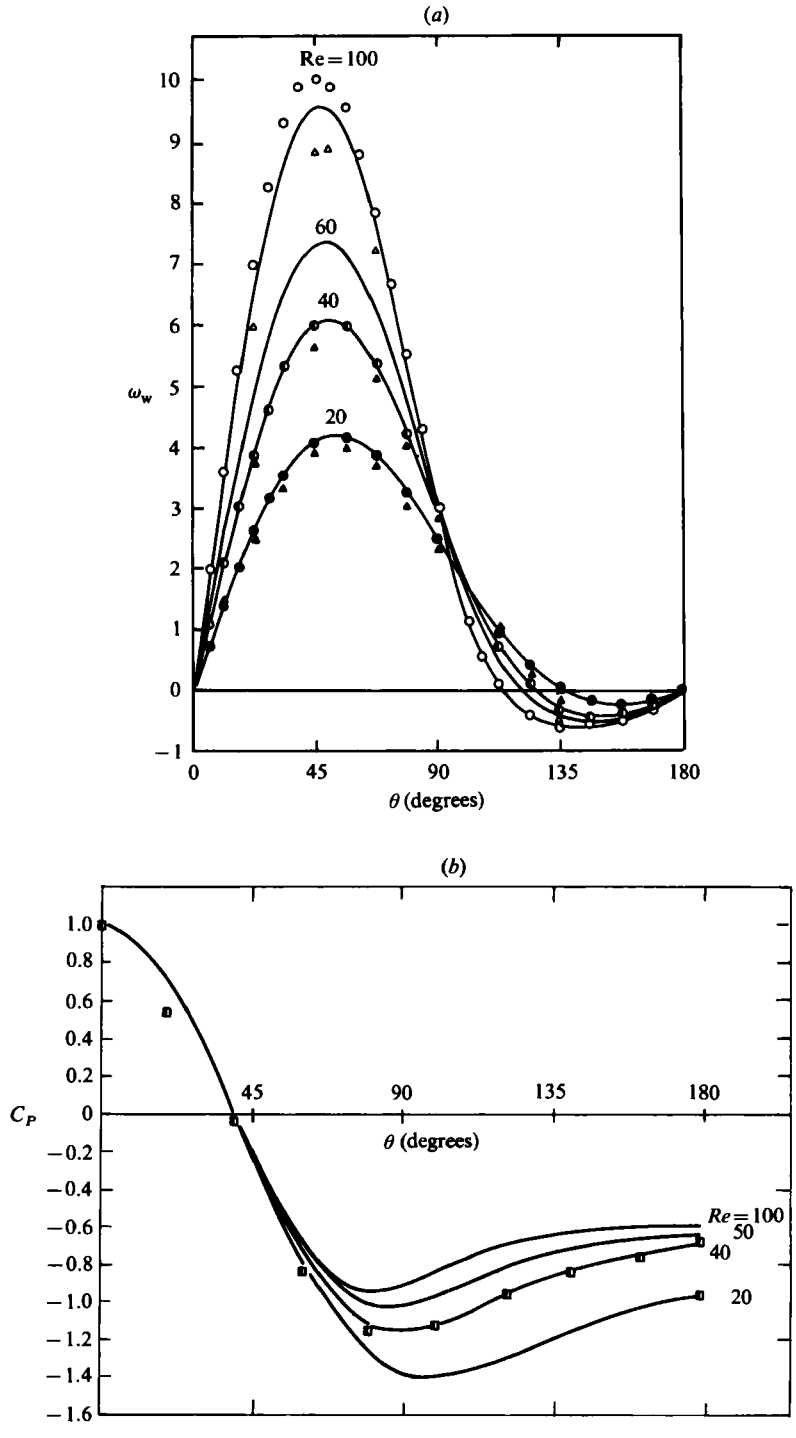

FIGURE 5. (*a*) Wall vorticity: ——, this study, Re = 20, 40, 60, 100. Martinez (1979): ●, Re = 20; ◐, 40; ○, 100. Fornberg (1980): ▲, Re = 20, ◭, 40, △, 100. (*b*) Wall pressure: ——, this study; ◧, experimental results of Grove *et al.* (1964), Re = 20 and 40.

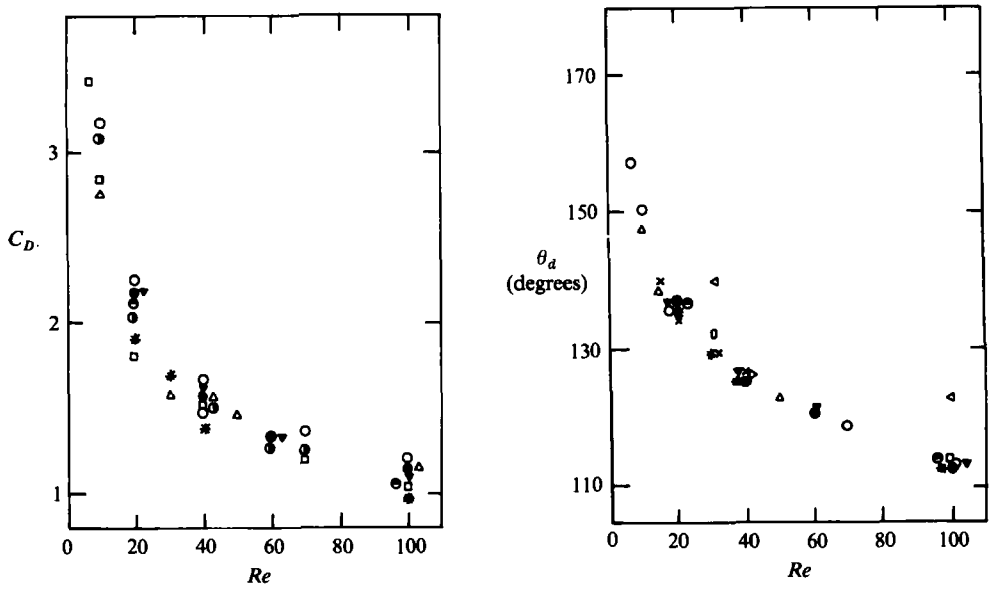

FIGURE 6. (*a*) Drag coefficient, (*b*) separation angle. Numerical results: ●, this study; *, Martinez (1979); □, Dennis & Chang (1970); △, Hamielec & Raal (1969); ○, Tuann & Olson (1978); ▼, Ta Phuoc Loc (1980); O, Thoman & Szewczyk (1969); ▷, Son & Hanratty (1969); ◓, Martinez & Ha Minh (1978). Experimental results: ◑, Tritton (1971); ×, Coutanceau & Bouard (1977); ◁, Grove *et al.* (1964).

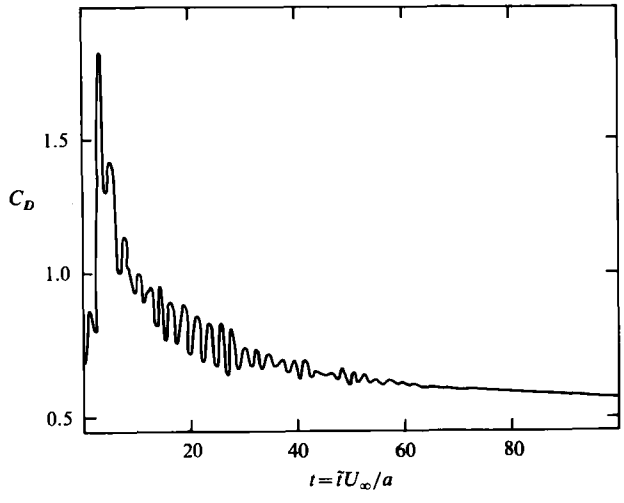

FIGURE 7. Time-dependent drag coefficient at $Re = 1000$.

(e.g. the surface roughness); perturbations in the running conditions of the experiment (e.g. vibrations).

In the case of the numerical simulation of the unsteady flow past a circular cylinder all these destabilizing effects are absent. As the geometry of the flow and the initial and boundary conditions are symmetric, the Navier–Stokes equations obviously lead to a symmetric solution even for values of Reynolds number greater than 40 (cf. Son & Hanratty 1969; Martinez 1979). The truncation and round-off errors, as well as those due to the numerical approximation schemes, are of course perturbating

factors, which could eventually generate vortex shedding. Nevertheless, numerical simulations for Reynolds numbers of 100 and 200 (Martinez 1979) and even up to 1000 (present study) have shown that the flow always achieves a steady symmetric pattern after a longer or shorter establishment period (figure 7).

The most reasonable way to generate vortex shedding should theoretically be to introduce into the physical model the same perturbations that occur during a physical experiment, if these perturbations were accurately prescribed. Unfortunately, it is not possible to know the characteristics of these perturbations in detail. Instead, it is rational to verify first of all that different kinds of numerically introduced physical perturbations lead to the same flow pattern: that of periodic alternating eddies, even if the corresponding establishment period is different. Secondly, the perturbation that provides the shortest establishment phase should be chosen to save computer time.

The numerical work of Martinez (1979), using a vorticity–stream function formulation, shows that different kinds of deterministic or random temporary perturbations are damped for Reynolds numbers less than 40, whereas they generate vortex shedding for Reynolds numbers of 50 and 100. The periodic flow pattern in this case is found to be similar to that reported from experimental studies, in spite of the fundamentally different nature of the perturbation between the physical and numerical models. Actually, the destabilizing factors in a physical experiment are not temporary but always present during the experiment and have a rather random occurrence. The fact that the numerical approach leads to the same flow pattern indicates that the periodic character of the flow appearing beyond a critical value of the Reynolds number is an intrinsic property of the Navier–Stokes equations and does not depend on the nature of the perturbations. Moreover, the perturbations seem only to be responsible for the change of the regime from steady to periodic flow, but they are not necessary as a source of energy to sustain the periodic flow. These two last points are quantitatively proven by the present numerical simulation.

In order to generate vortex shedding two artificial perturbations are tested for $Re = 100$, both introducing a rotation of the circular cylinder for a short time (figure 8*a*). The perturbations introduced correspond to a clockwise rotation of the cylinder followed by a counterclockwise rotation. They are of the same nature as those used by Martinez (1979). The first perturbation shows a rather long transition period: the flow did not reach a strictly periodic state within the investigation time (figure 8*b*). Nevertheless the oscillations of the lift coefficient give a value of the Strouhal number of 0.16, in agreement with many of the experimental results referred to below. As the second perturbation (figure 8*c*) initiates periodic vortex shedding earlier with the same final dynamic characteristics (Strouhal number), it will be used for all the calculations.

The periodic properties of the flow are clearly shown by the time-dependent evolution of the lift coefficient. In fact the mean value of the lift coefficient for a symmetric body in uniform flow is zero. This can be observed in figure 8(*c*). The frequency of the oscillations in terms of the dimensionless Strouhal number is found to be 0.16. This result agrees with the experimental values reported by Roshko (1954) and Tritton (1959), as well as with the numerical results of Jordan & Fromm (1972) and Martinez (1979).

The evolution of the lift coefficient for Reynolds numbers of 200 and 1000 are shown in figures 8(*d*, *e*). The periodic character of the flow is also well predicted in these cases. The corresponding values of the Strouhal number are 0.20 and 0.21. The numerical work of Ha Minh, Boisson & Martinez (1980) based on a vorticity–stream function formulation reports the value of 0.19 for $Re = 200$.

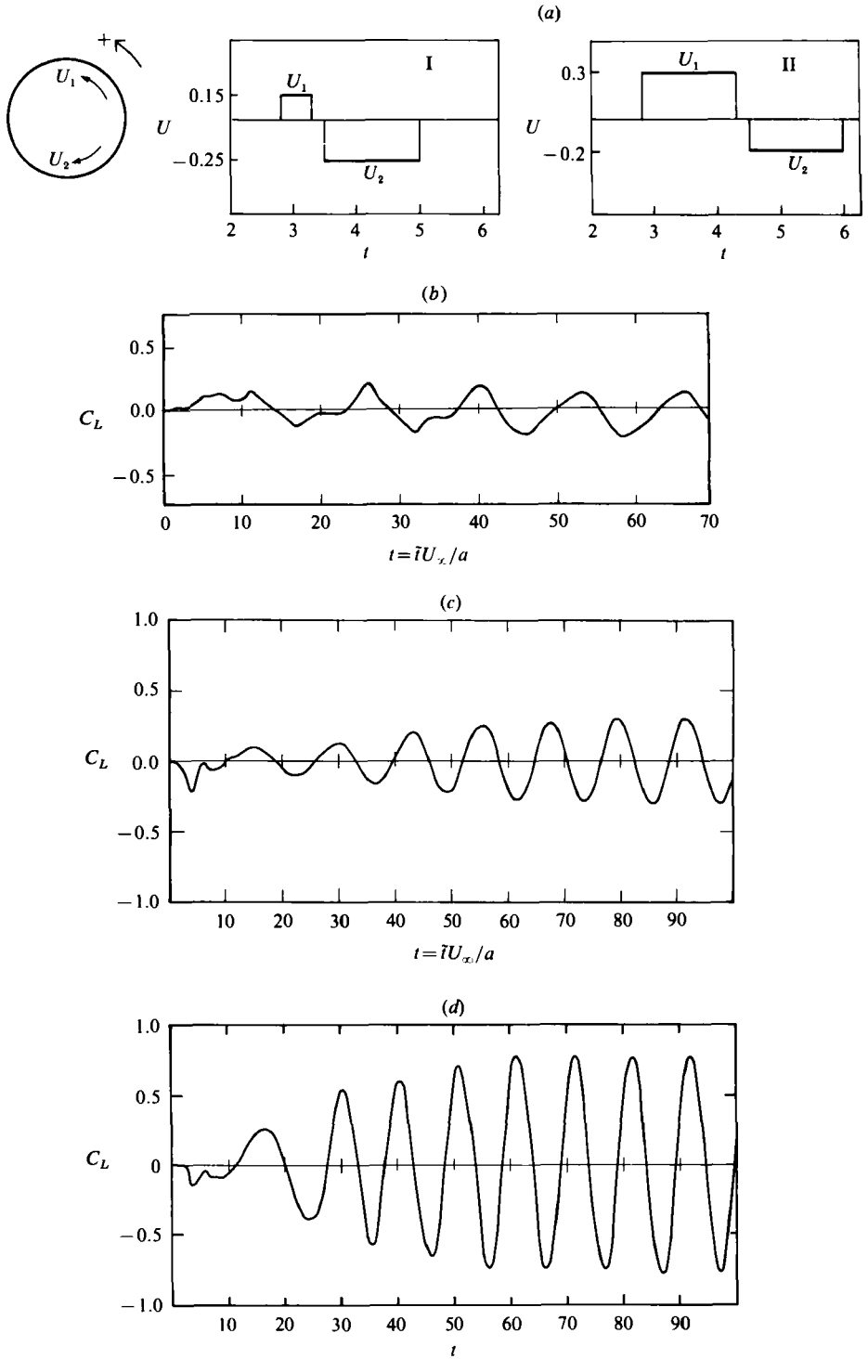

FIGURE 8. (*a*) First and second perturbations. Variation of the wall tangential velocity, as a function of time. (*b*) First perturbation. Time-dependent lift coefficient for $Re = 100$. (*c*) Second numerical perturbation. Time-dependent lift coefficient for $Re = 100$. (*d*) Time-dependent lift coefficient for $Re = 200$. (*e*) Time-dependent lift coefficient for $Re = 1000$.

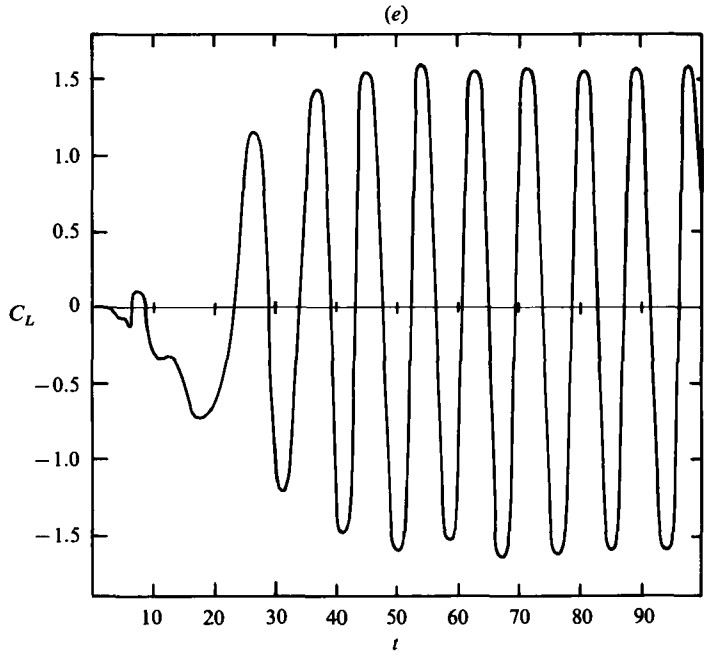

FIGURE 8(*e*). For description see facing page.

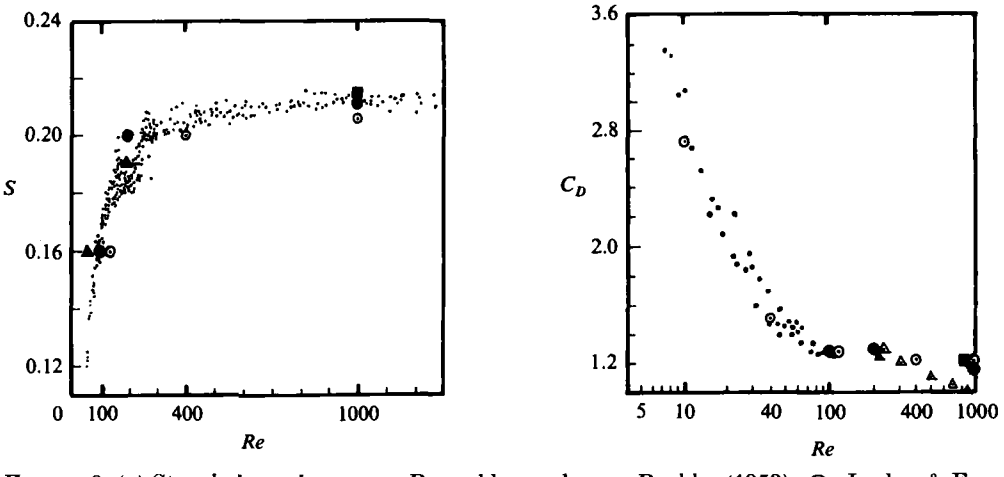

FIGURE 9. (*a*) Strouhal number *versus* Reynolds number: ·, Roshko (1953); ⊙, Jordan & Fromm (1972); ▲, Martinez (1979); ■, present results, (*a*) (see table 1); ●, present results, (*b*) (see table 1). (*b*) Mean drag coefficient *versus* Reynolds number: ·, Tritton (1959); △, Wieselsberger (1921); ⊙, Jordan & Fromm (1972); ■, present results, (*a*) (see table 1); ●, present results, (*b*) (see table 1).

Experimental results of Roshko (1954) give quite dispersed values for the Strouhal number, in the range 0.18–0.20, for the same Reynolds number. The reason for this is probably the beginning of laminar–turbulent transition due to an instability in the shear mixing layer downstream of the separation point, as reported in the above experimental work, among others. These turbulent features could not be predicted by the present code, but only the global characteristics of the flow, such as the drag

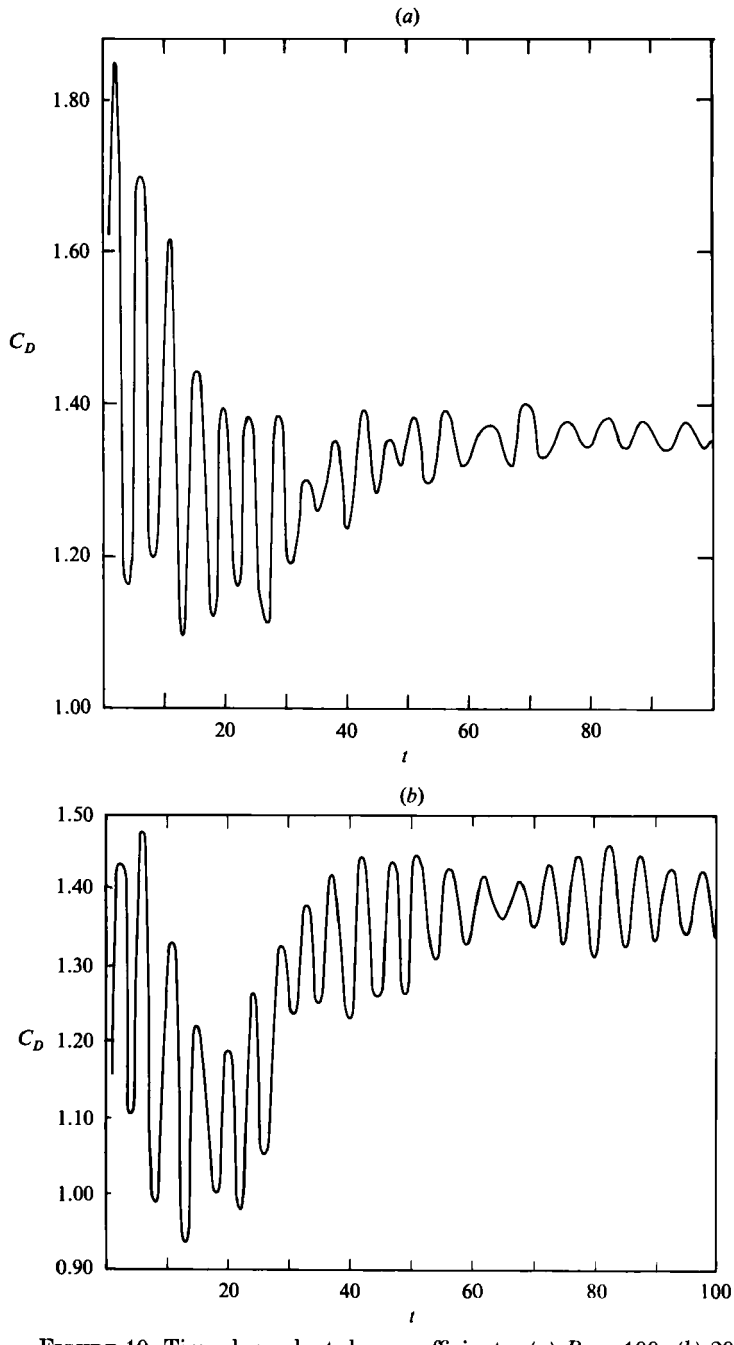

FIGURE 10. Time-dependent drag coefficients: (*a*) $Re = 100$; (*b*) 200.

and lift evolutions and a mean value of the Strouhal number, deduced from the near-wall parameters. The computed values of the Strouhal number and of the mean drag coefficient *versus* the Reynolds number are presented in figures 9(*a*, *b*). Results for the two sets of numerical parameters for $Re = 1000$ ((*a*) and (*b*) of table 1) are shown, giving both values close to experimental ones: (*a*) $St = 0.217$, (*b*) $St = 0.21$ and (*a*) $C_D = 1.21$, (*b*) $C_D = 1.198$. The second set is finally retained, in order to

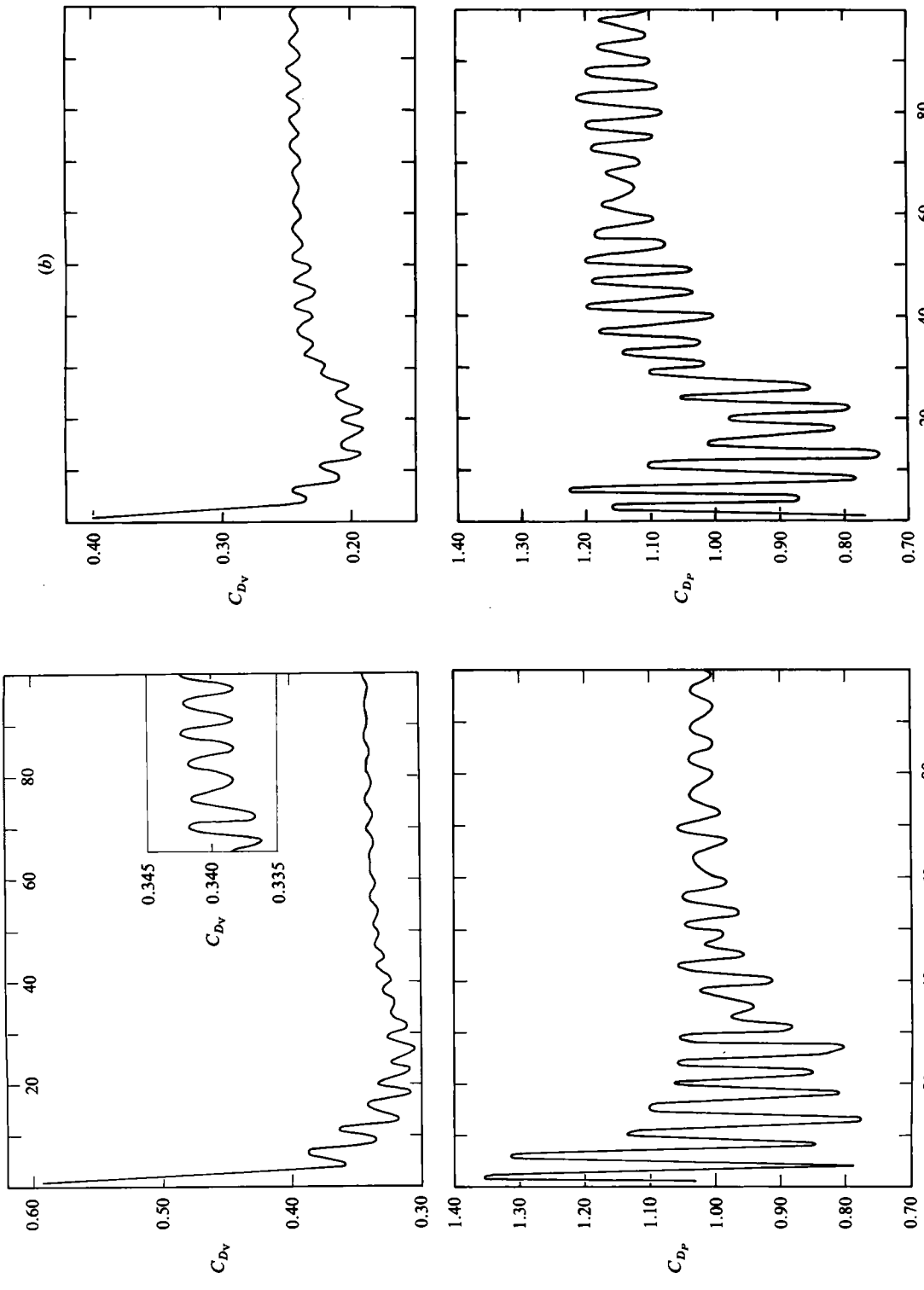

FIGURE 11. Viscous and pressure drag coefficients: (*a*) $Re = 100$; (*b*) 200.

	θ (degrees)			θ (degrees)	
t	(a)	(b)	t	(a)	(b)
80	114.88	114.56	87	114.05	114.22
81	117.17	116.92	88	112.96	113.01
82	119.56	119.21	89	112.41	112.53
83	120.23	119.96	90	112.56	112.64
84	119.19	119.00	91	113.60	113.51
85	117.13	117.35	92	115.22	115.02
86	115.45	115.51			

TABLE 2. Values of the separation angle in a period for $Re = 100$, according to the vanishing wall vorticity (a), and the vanishing shear stress in the boundary layer (b) criteria

provide a better resolution. A good agreement of St and C_D with experimental results is obtained for all Reynolds numbers.

The periodic character of the flow is less obvious in the time-dependent evolution of the drag coefficient (figures 10a, b). Actually, the drag force is a result of the convective motion of the cylinder through the fluid. Because of this motion and of the non-slip condition at the wall, a tangential velocity gradient is created in the direction normal to the wall.

The value of this gradient near the separation point changes following the oscillations of the separation point forward and backward (see figure 17). Owing to the convective motion, there is a preferential direction of the flow even in the vicinity of the separation. For this reason, the time-dependent evolution of the tangential velocity gradient and, consequently, of the wall vorticity, are not strictly sinusoidal. Also, the drag coefficient is a function of wall vorticity multiplied by $\sin x$, whereas lift coefficient is a function of wall vorticity and $\cos x$ (cf. (37) and (38)). The values of $\sin x$ are higher than those of $\cos x$ near the separation points. Hence, the effect described above is more pronounced in the drag coefficient evolution, than in time-dependent lift coefficient. Moreover, the establishment time for the drag coefficient is found to be longer than the corresponding time for the lift coefficient.

The frequency of the drag-coefficient oscillations is found to be twice that of those of the lift coefficient. This result is due to the contribution of the upper and lower alternating vortices to the drag effort. The total drag is also due to two effects: the pressure field (C_{D_P}) and the viscous forces (C_{D_V}) calculated by the relations (36)–(38). Figures 11(a, b) show the time-dependent viscous and pressure components of the drag coefficient and the pressure contribution is seen to predominate. For $Re = 100$ the mean value of the pressure drag is 1.02, which corresponds to 80% of the total drag. This value is found to be close to the experimental results of Roshko (1954) ($C_{D_P} = 0.995$).

The pressure and viscous drag coefficients oscillate with the same frequency as the total drag coefficient. Their oscillations are found to be almost in phase.

The averaged total drag coefficient (figure 9b) is found to be higher than that corresponding to the steady state at the same value of the Reynolds number. For $Re = 100$ $C_D = 1.28$ in the oscillating flow, whereas $C_D = 1.17$ (cf. figure 6a) for the steady flow. The rise in the mean drag on the unsteady case is also reported by Jordan & Fromm (1972).

The mean value of the unsteady drag for $Re = 100$ calculated by the present method is close to the experimental results of Tritton (1959). This fact leads us to suppose

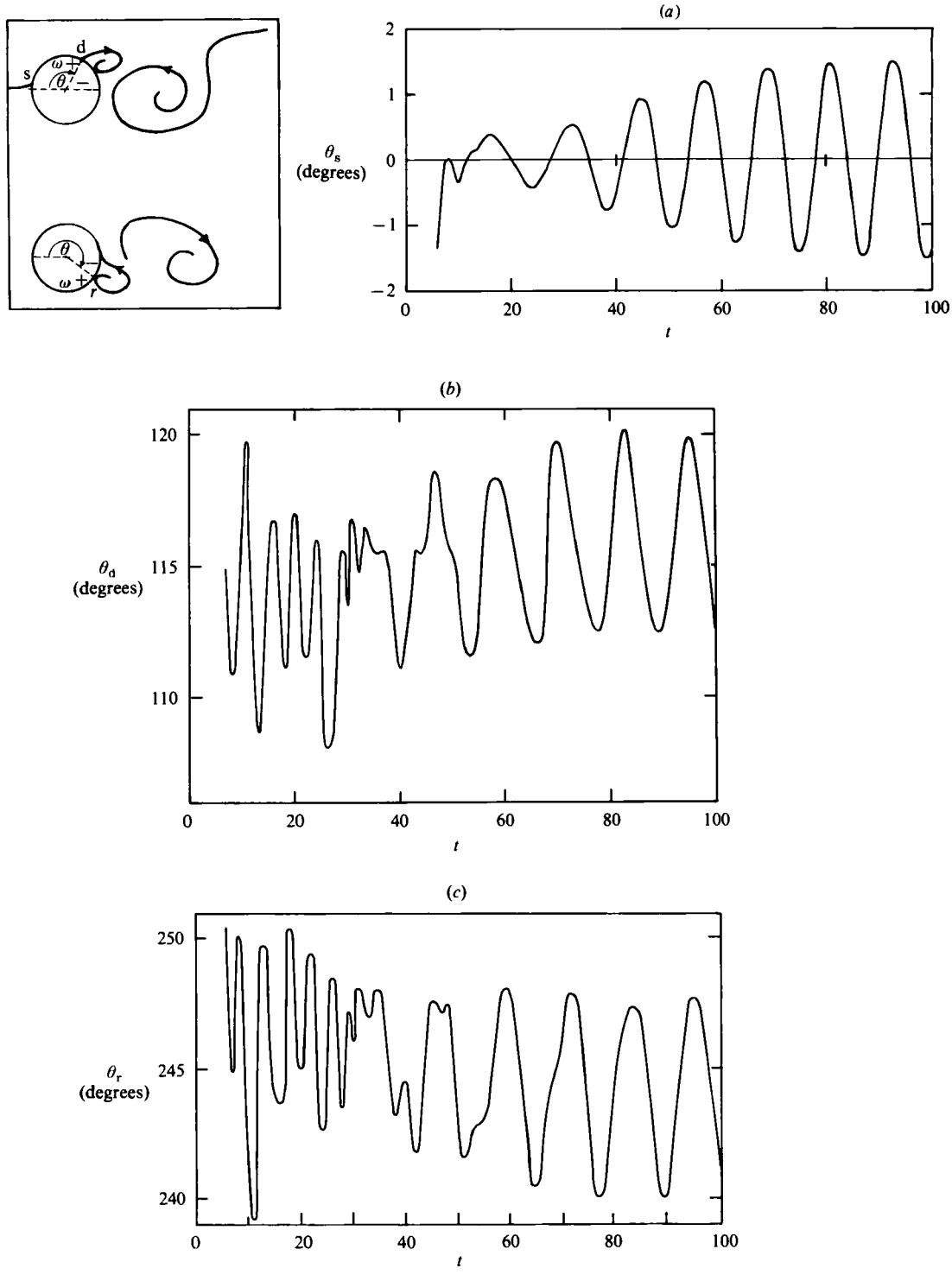

FIGURE 12. (*a*) Time-dependent (*a*) stagnation, (*b*) separation and (*c*) reattachment angles for $Re = 100$.

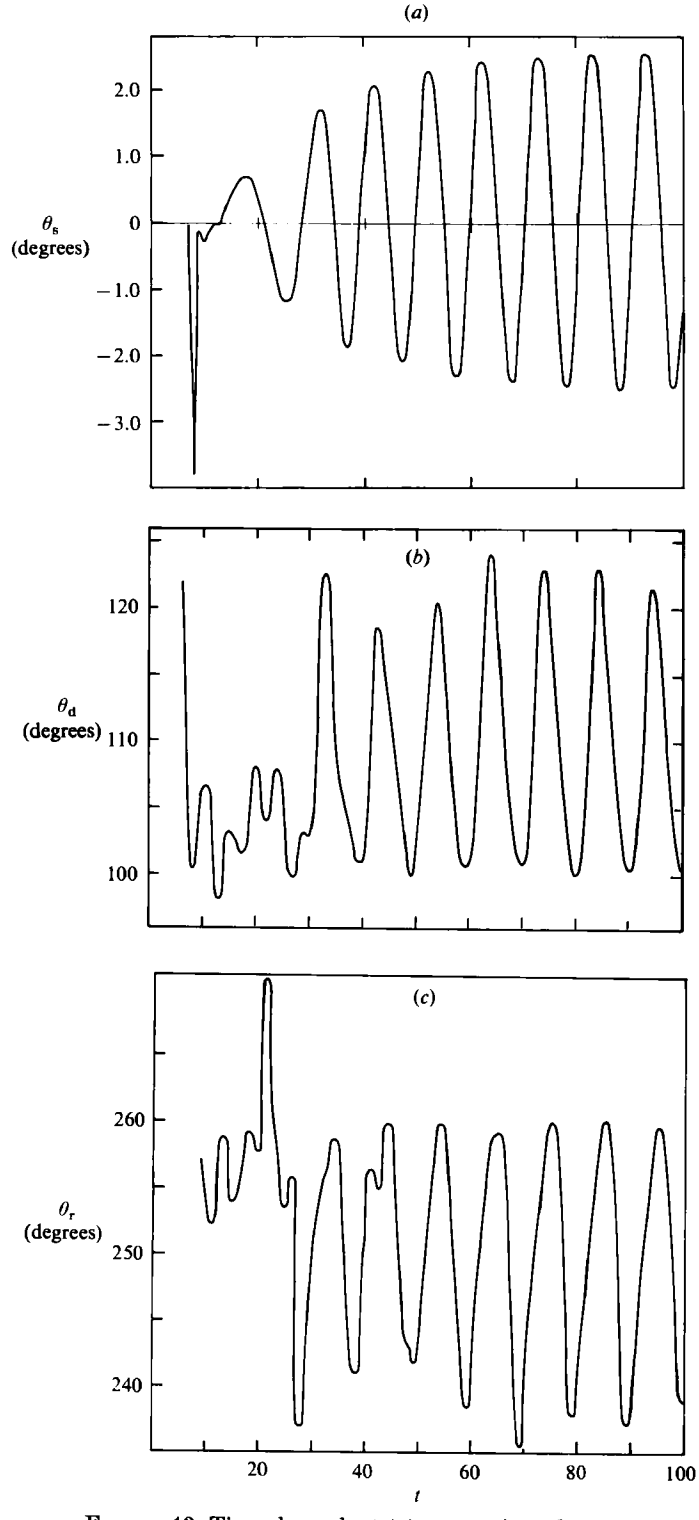

FIGURE 13. Time-dependent (*a*) stagnation, (*b*) separation and (*c*) reattachment angles for $Re = 200$.

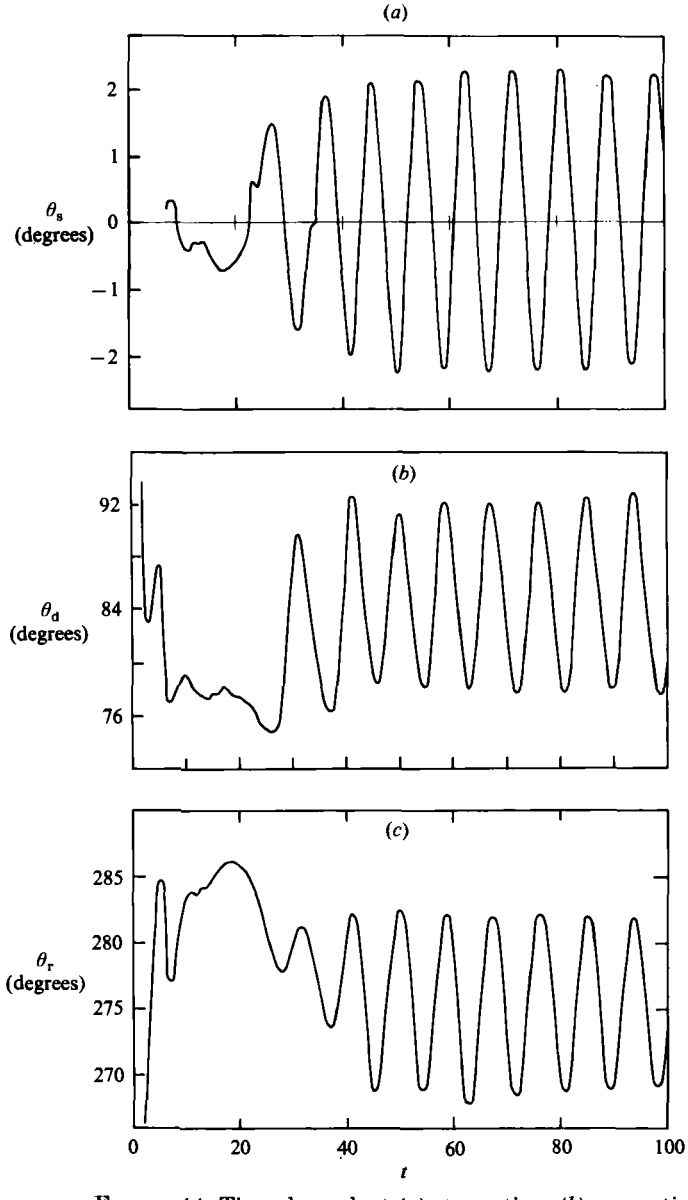

FIGURE 14. Time-dependent (*a*) stagnation, (*b*) separation and (*c*) reattachment angles for $Re = 1000$.

that the steady symmetric case is not a realistic description of the flow, but rather a mathematical concept.

The stagnation, separation and reattachment angles correspond to points of zero wall vorticity (points s, d and r of figure 12*a*), in the present work. If the wall vorticity, $\omega_w = (\partial u/\partial y - \partial v/\partial x)\, a/U_\infty$, is positive below zero and negative above zero, the point corresponds to separation, as sketched by the streamline in the same figure. If the wall vorticity is negative below zero and positive above zero, the corresponding point is a reattachment one. Nevertheless, the above definition of separation point is exact only for a steady flow. In an unsteady flow, the exact separation point should

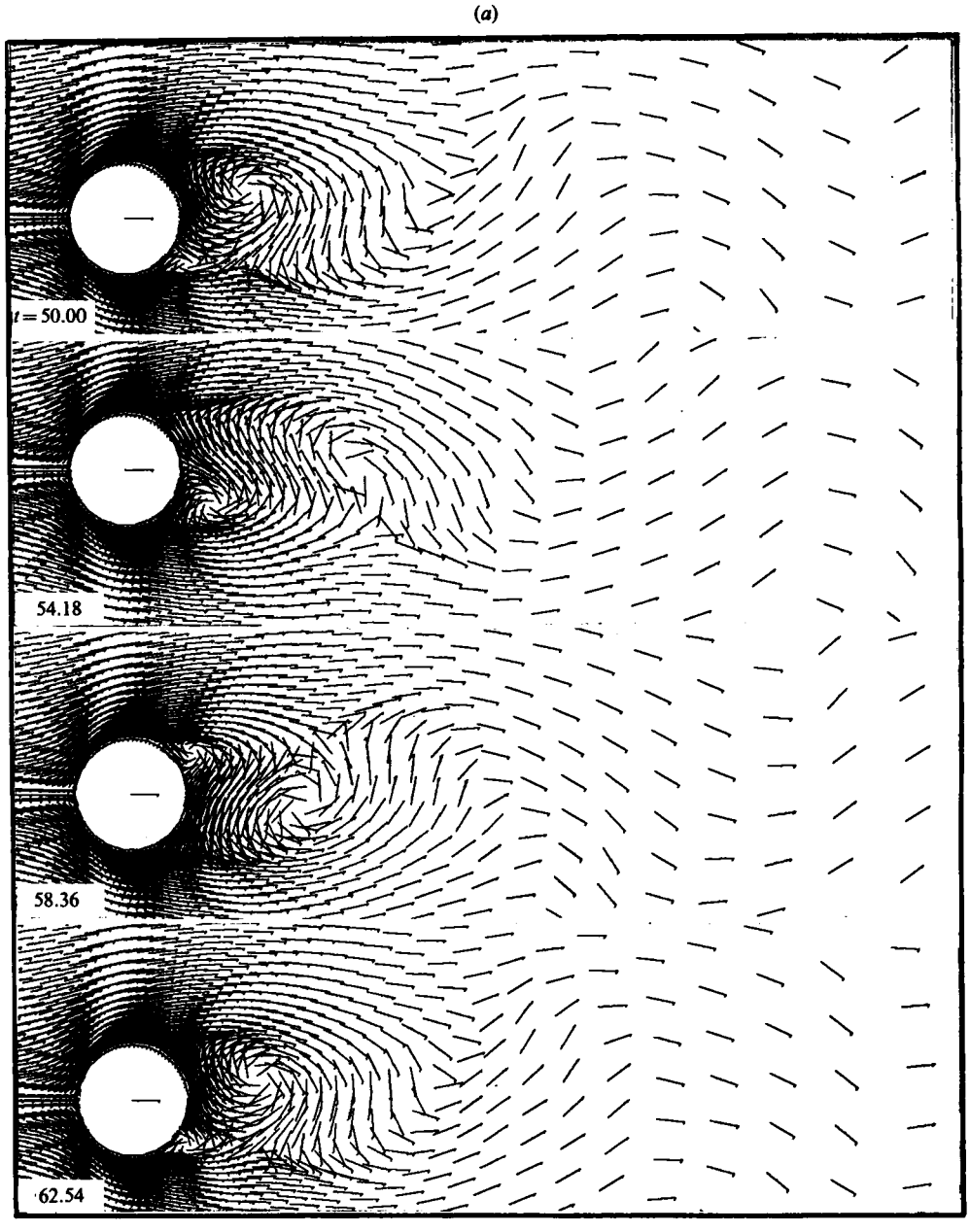

FIGURE 15. Instantaneous velocity fields: (*a*) $Re = 100$; (*b*) 200.

be defined as the point of simultaneous vanishihg of the shear stress and velocity at a point within the boundary layer (Sears & Telionis 1975). Results using both methods have been checked for $Re = 100$ and found to have a discrepancy of less than 0.3 % (see table 2).

The stagnation, separation and reattachment angles also oscillate periodically (figures 12–14). Their frequency corresponds to the Strouhal number of each lift coefficient.

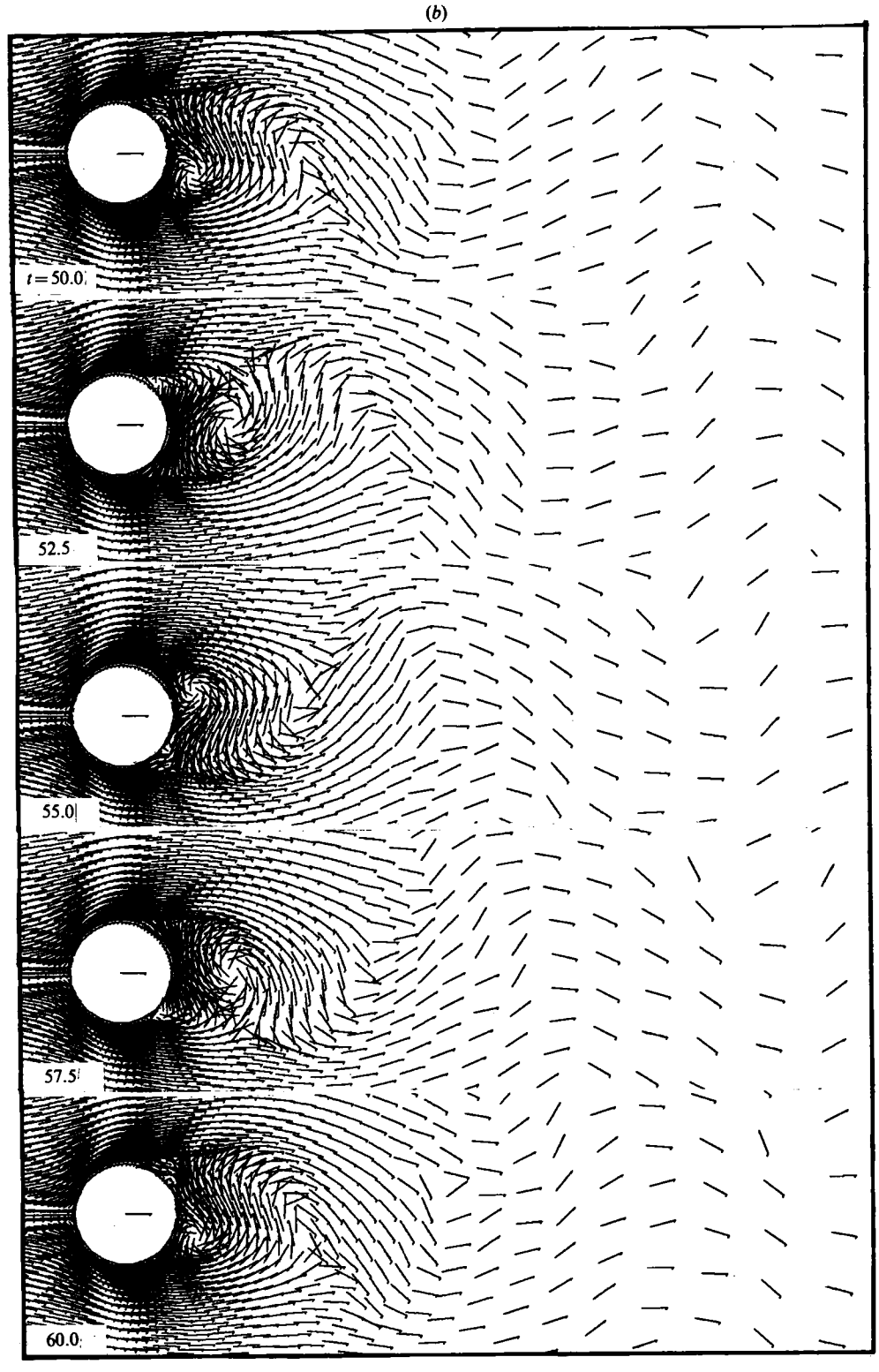

FIGURE 15(*b*). For description see facing page.

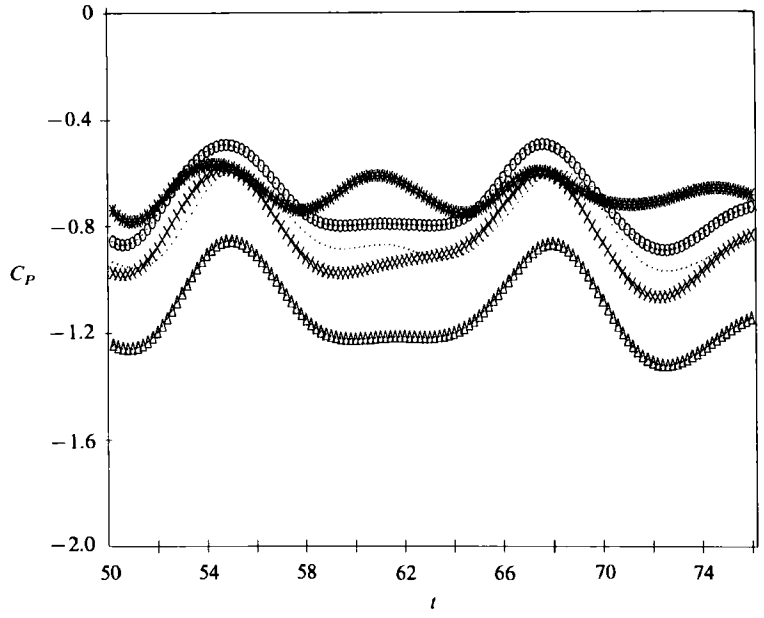

FIGURE 16. Time-dependent wall pressure coefficient. Angle values: ....., $\theta = 67.75°$; , 87.75°; 119.25°; , 150.75°; 177.75°.

In figures 15(*a*, *b*) the directions of the velocity vectors are plotted at four ($Re = 100$) and five ($Re = 200$) phases of a period. The alternating formation, convection and diffusion of the vortices is clearly shown. At $Re = 1000$ different flow phenomena develop and so the description will be deferred until the next section.

The results discussed in this section show that vortex shedding is an intrinsic phenomenon of the flow, well predicted by the solution of the Navier–Stokes equations. It is the response of the dynamic system to the existing perturbations and does not depend on the details of those perturbations. The flow system has, then, a strongly deterministic character. The vortex shedding is generated by a loss of symmetry of the two-dimensional symmetric structures in the wake of the circular cylinder, above a critical value of the Reynolds number, owing to physically existing perturbations. It constitutes a bifurcation of the solution of the Navier–Stokes equations, approaching transition.

4.3. *Analysis of interactions of the velocity and pressure fields*

The principal goals of this paragraph are to study the influence of the viscous forces in the near-wake region on the unsteady pressure field related to the velocity field, the behaviour of these fields in the irrotational region, and the influence of vortex shedding (formation and convection regions of the alternating eddies) on the pressure and velocity interactions.

Essentially these aspects are investigated using phase differences and amplitude variations of the time-dependent evolution of the pressure and velocity: (*a*) on the wall (pressure); (*b*) outside the wake ($\theta = 90°$); and (*c*) in the wake ($\theta = 153°$). The time interval taken is slightly greater than two periods. This study is carried out for $Re = 100$.

The time-dependent wall-pressure coefficient, $C_P = (P - P_\infty)/0.5\rho U_\infty^2$, is given in figure 16. The minimum values of the pressure are found to be less steep than the

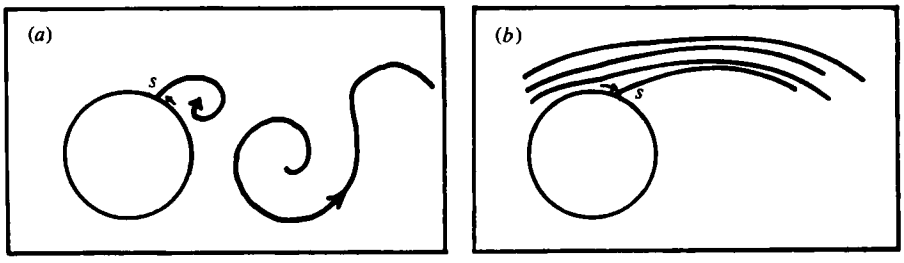

FIGURE 17. Sketch of the flow pattern associated with the motion of the separation point.

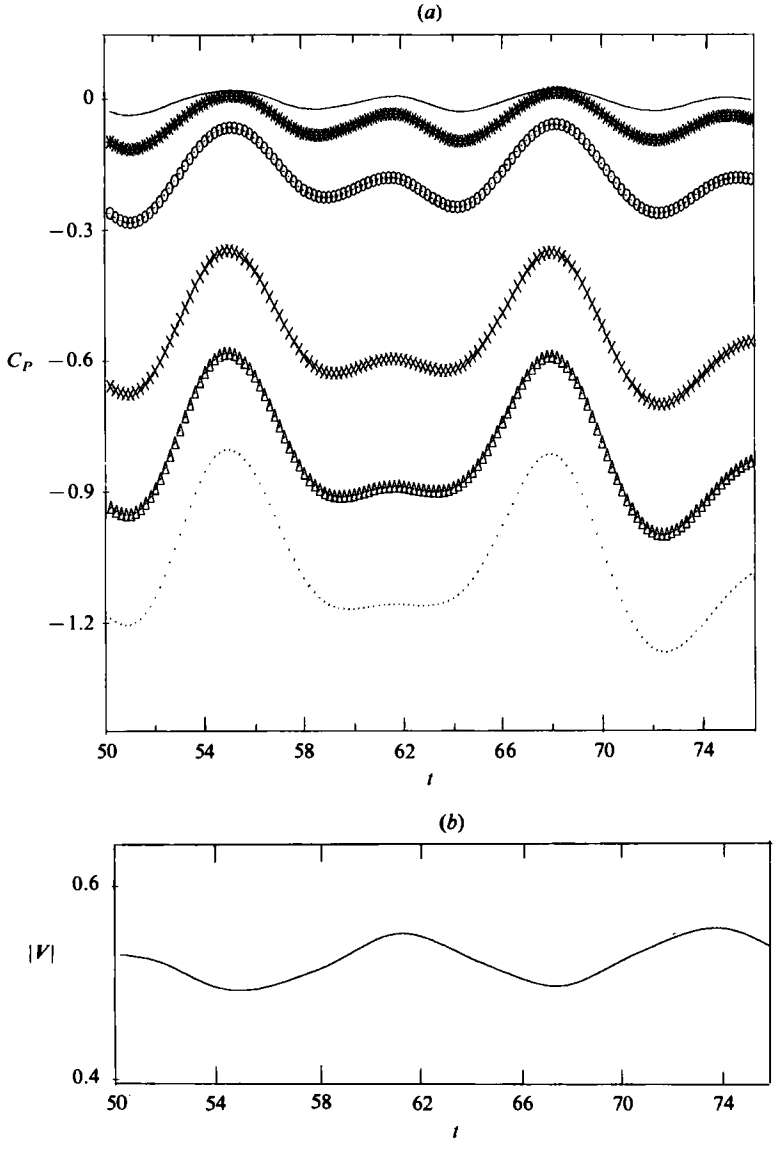

FIGURE 18. (*a*) Time-dependent pressure coefficient at $\theta = 87.75°$; ....., $r/D = 0.56$; , 0.71; , 0.90; , 1.82; , 3.85; ——, 9.32. (*b*) Time-dependent velocity modulus at $r/D = 0.56$, $\theta = 90°$.

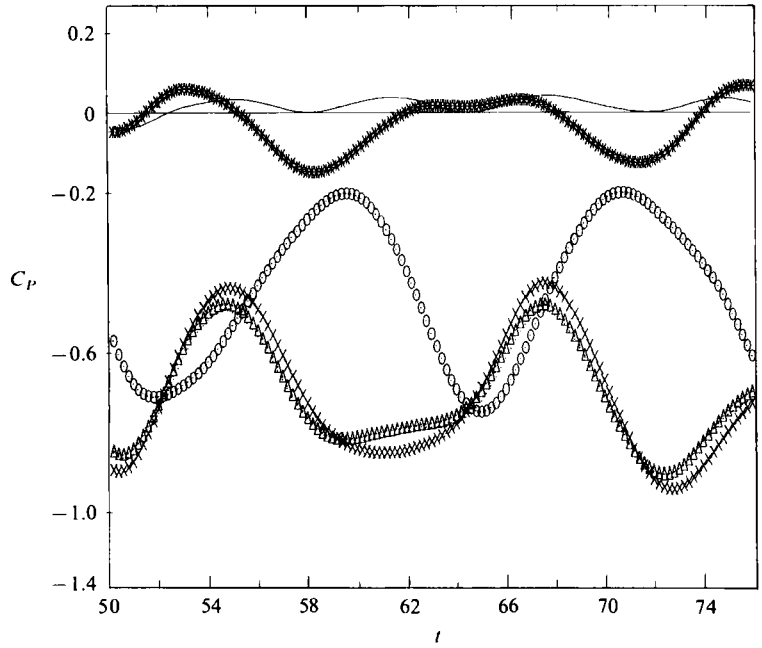

FIGURE 19. Time-dependent pressure coefficient at $\theta = 150.75°$. Symbols as in figure 18(*a*).

maximum ones for all the angular positions investigated, except for $\theta = 177.75°$, which corresponds to the vicinity of the rear axis. The pressure oscillates twice as fast there as the lift coefficient because of the simultaneous contribution of both the alternating vortices. The presence of the first harmonic frequency is also clearly shown. The maximum values of the wall pressure are not in phase. Their shift is calculated by taking the angle $\theta = 60.75°$ as a reference. The corresponding values of the phase angle are 12°, 23°, 23° and 40°.

The variations of the wall pressure are not symmetric relatively to their mean value. This could be explained by the two kinds of flow pattern associated with the motion of the separation point (figure 17). Even if the separation angle oscillates quite periodically around its mean value, two dynamically different positions could be distinguished. In the first case (lower values of the separation angle, figure 17*a*), there is always an alternating vortex in the vicinity of the separation point. The occurrence of this vortex is periodic. In the second case (higher values of the separation angle, figure 17*b*) the points previously having been in a recirculating region are actually in a strongly convective, almost steady, motion. Hence the oscillations of the pressure coefficient are different in the two cases. They become more periodic as θ increases and tends to 180°, i.e. for points in the fully developed-wake region.

The mean value of the wall-pressure coefficient at the rear axis is −0.668. The numerical results of Jordan & Fromm (1972) deduced from ψ–ω calculations give a value of 0.66 and the experimental results of Acrivos *et al.* (1965) 0.60.

In order to study the effects of the viscous and irrotational zones on the pressure and velocity outside the wake, the time-dependent pressure coefficient is plotted at six radial positions on the line $\theta = 87.75°$ (figure 18). The unsteady velocity at $\theta = 90°$ is plotted for only one radial position near the wall (figure 18*b*) since its fluctuations are found to be very low compared with those of the pressure in the outer

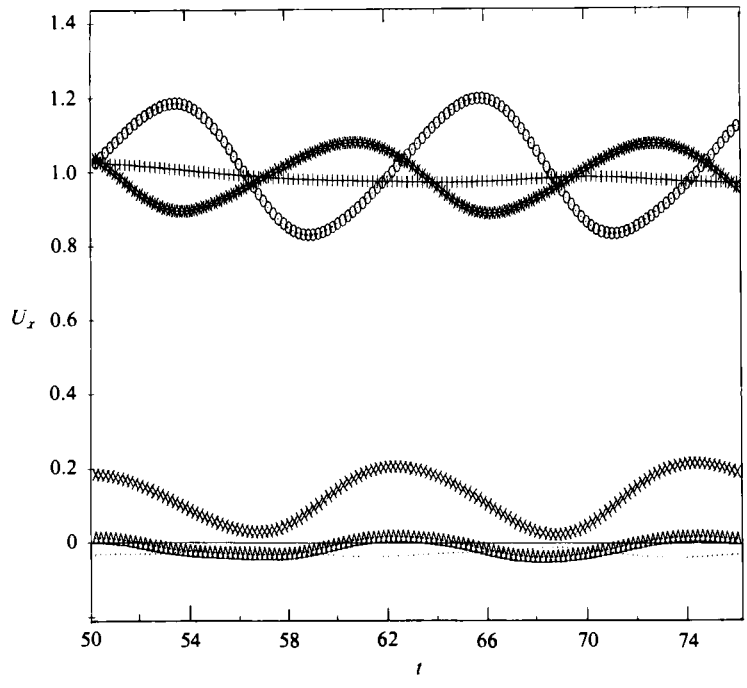

FIGURE 20. Time-dependent U_x component at $\theta = 153°$. Symbols as in figure 18(*a*); ||||||||, $r/D = 9.32$.

region. The corresponding orders of magnitude of fluctuations are approximately 2 % of U_∞ for the velocity modulus and 15 % of ρU_∞^2 for the pressure. The velocity is close to the uniform-flow value. Also, pressure fluctuations are weaker than in the near-wall region. Nevertheless, they are not as much attenuated as those of the velocity. The periodic character of the flow is transmitted through the pressure field, even at a large distance from the wall, like an acoustic wave. Far from the wall the diffusion term, ν div (grad $\boldsymbol{V}$), is low and the convective forces $\boldsymbol{V}$ grad $\boldsymbol{V}$ vary like grad P. The fluid moves then as a block; hence the pressure variations are in phase ($r/D = 3.85$ and 9.32). For the same reason, the fluctuations are more regular than near the wall, indicating a strongly periodic movement.

This suggests that such a signal could be used as a trigger criterion of the vortex-shedding phase, whenever a conditional (phase)-averaged analysis is to be performed. This technique is used by numerous experimental studies, e.g. Boisson, Chassaing & Ha Minh (1983). For the turbulent-flow Reynolds numbers the distance beyond which a regular periodic character of the flow can be found is obviously smaller than the approximate value $r/D = 3{,}85$ corresponding to the $Re = 100$ case.

Along the line $\theta = 87.75°$ the pressure forces are balanced by the convection and the viscous forces, the influence of the first being stronger beyond $r/D \gtrsim 1.82$ and the effects of the second being important for $r/D < 1.82$. This balance leads to higher amplitudes for the pressure near the wall, where the velocity is small, and lower amplitudes far from the wall, where the velocity modulus is high. For the same reason the fluctuations of the velocity and pressure are found to be out of phase by approximately 180° (figure 18*b*, $r/D = 0.56$). The viscous forces are responsible for the loss of the periodic character near the wall. They affect somewhat the minima of the pressure variations by attenuating the influence on the frequency of the lower

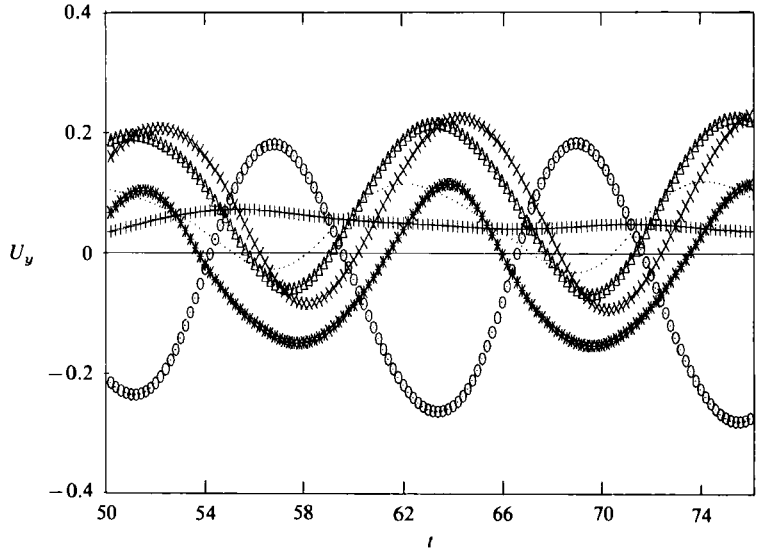

FIGURE 21. Time-dependent transverse velocity component U_y. Symbols as in figure 18(*a*).

alternating eddies. In fact the maximum amplitude in the time interval (58, 66) at $r/D = 0.56$ is less apparent than at $r/D = 3.85$ and 9.32. These two last positions are far from the influence of both the alternating eddies and the viscous forces and hence they oscillate regularly and with a frequency twice that of the pressure at $r/D = 0.56$. It is also noticeable that the viscous forces do not create phase shifting of the pressure fluctuations. In fact, the maxima of these fluctuations are found to be in phase along $\theta = 87.75°$ for all the radial positions investigated. This is due to the absence of convection of vortices at $\theta = 87.75°$ (see also figure 15*a*). As it is shown in the following, the convection of eddies in the wake is responsible for a phase shifting of the pressure and velocity fluctuations.

In order to examine the effects of the formation and convection of the eddies on the interactions of the pressure and velocity fields, the time-dependent pressure coefficient is plotted for the same values of r/D as previously and at $\theta = 150.75°$ (figure 19). The velocity components U_x and U_y in the directions of the classical Cartesian coordinates, and the velocity modulus, are also plotted at $\theta = 153°$ (figures 20–22).

The different values of the angle correspond to two adjacent mesh points for the pressure and velocity and are due to the staggered grid. Interpolations in order to calculate the pressure and velocity at the same point are avoided for the present analysis to maintain the accuracy achieved by the numerical method. The values of r/D related to an instantaneous location of the eddies is shown in figure 23.

The irrotational behaviour of the flow, as discussed for $\theta = 87.75°$, is again found at $r/D = 9.32$. Obviously a longer distance ($r/D = 9.32$) is necessary to reach the almost irrotational region than the corresponding distance at $\theta = 87.75°$ ($r/D = 3.85$). Nevertheless, the value of $r/D = 9.32$ could not be used as an external radius for the computations. At $\theta = 180°$, because of the strongly elliptic character of the flow due to incompressibility and viscous effects, the above external radius is not sufficiently far from the wall and so influences the near-wake field. It is found by numerical tests that the minimum value of R_∞/D for which boundary condition does not affect the near-wake flow field is 57.27.

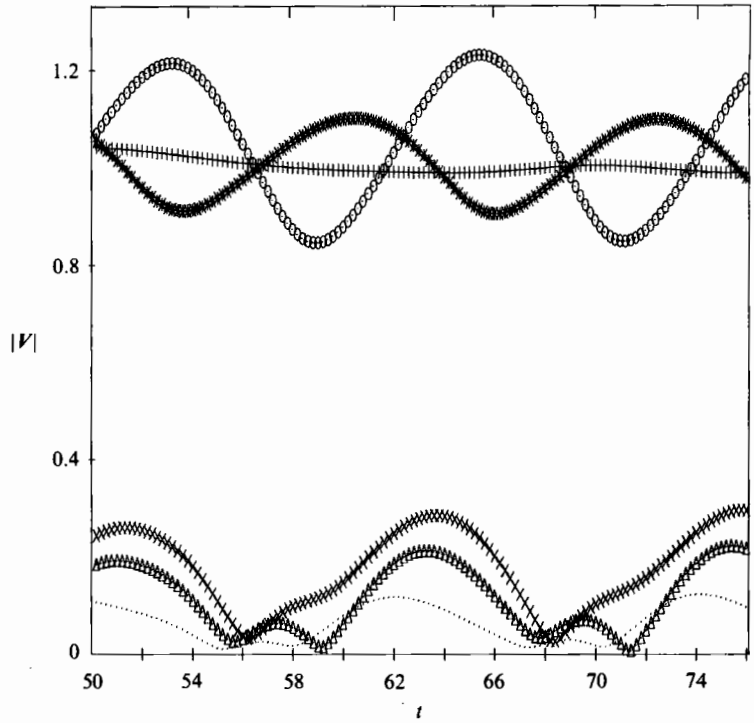

FIGURE 22. Time-dependent velocity modulus at $\theta = 153°$. Symbols as in figure 18(*a*).

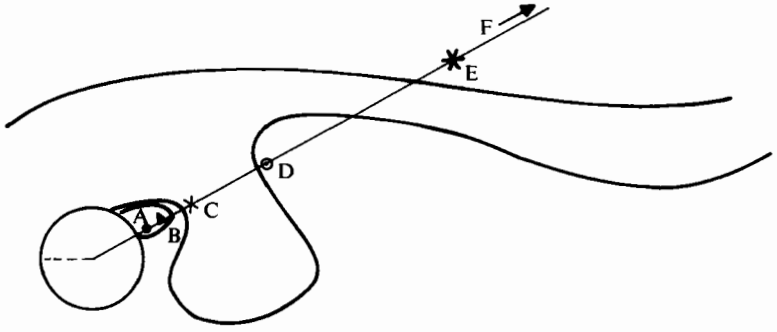

FIGURE 23. r/D values and corresponding points in the wake, at $\theta = 153°$. A, $r/D = 0.56$; B, 0.71; C, 0.90; D, 1.82; E, 3.85; F, 9.32.

The balance between the different terms of the conservation of momentum (pressure, convection and diffusion) explain the fact that the pressure evolution is opposite in phase to the corresponding velocity at the same r/D values (figure 24).

The viscous effects near the wall are responsible here too for the loss of symmetry in the pressure evolutions relatively to their mean value. The new element for the present position is the phase lag observed between two adjacent r/D values of the pressure and velocity evolution. This can be explained in relation to the convection of the eddies.

The phase lag of the pressure coefficient is rather small in the near wake ($r/D = 0.56$ and 0.71). In fact, these two positions are in the same eddy, located in the formation area, where convection is low (points A and B in figure 23). Hence, the transfer of

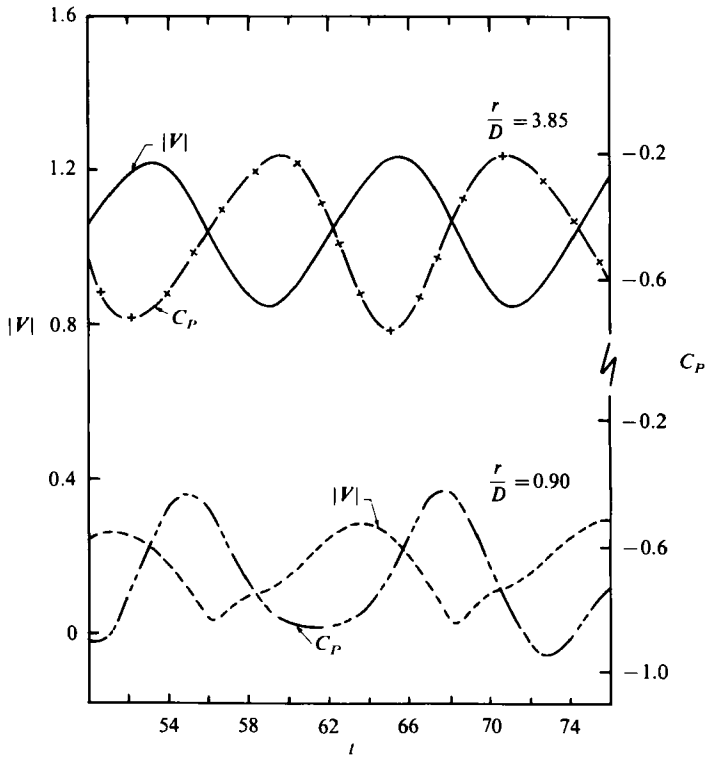

FIGURE 24. Phase relations between pressure and velocity fluctuations at $\theta = 153°$.

properties such as the velocity and pressure occurs almost simultaneously. The oscillations of the pressure are then almost in phase at $r/D = 0.56$ and 0.71.

The phase shifting increases for points far from the wall and reaches the value of 63° for $r/D = 1.83$, taking $r/D = 0.56$ as the reference point. This phase difference is due to the convection of the eddies (points A and C, figure 23). The corresponding convective velocity, defined as

$$U_c = \frac{2r\cos\theta}{D(t_2 - t_1)} \tag{39}$$

is equal to 0.78, where r is the distance between points A and C, D the diameter of the cylinder, and $(t_2 - t_1)$ the time interval between the maxima of the pressure coefficients. This value is close to that reported by many experimental studies for a large number of Reynolds numbers covering the subcritical regime.

Because of the relative positions of points C and D, the corresponding pressure fluctuations are almost in phase opposition (figure 19). Convection is also responsible for a loss of symmetry in the evolution of the pressure oscillations relative to their mean value: examining the pressure fluctuations for points C and D, it is found that the evolution of the pressure at C is more nearly symmetric than that at D. In fact, C is outside the wake, whereas D is in it.

The recirculating regions in the wake also create a strong fluctuating behaviour in the U_x, U_y and V evolution (figures 20 to 22), even far from the wall.

The main points of the discussion in this section can be summarized as follows:

The velocity and pressure fluctuations are found to be almost in phase opposition in the whole field.

The viscous effects create a loss of symmetry of the pressure and velocity evolutions, relative to their mean values, and a slight phase shifting (figure 24) such that the pressure and velocity fluctuations are deviated from the phase-opposition relation near the wall.

The convection of the alternating eddies enhances a phase lag in the pressure and velocity fluctuations. The value of this lag gives a global convective eddy velocity of 0.78.

4.4. *Analysis of the behaviour of different types of structures in the near wake*

The pattern of the periodic flow with vortex shedding was described in §4.2 for the Reynolds-number range 100–1000. The generation of vortex shedding has been achieved by imposing the same numerical perturbation (figure 8*a*) for all cases. The global periodic character of the flow is found to be essentially the same as the Reynolds number increases. For a Reynolds number of 1000 it should be recalled that the unsteady lift coefficient (figure 8*d*) oscillates periodically and gives a Strouhal number of 0.21 (figure 9*a*). Nevertheless, a finer analysis of this flow reveals a different type of structure in the near-wall region. Apart from the formation of the classical alternating eddies, one particular feature is the presence of pronounced secondary vortices in the vicinity of each primary eddy.

Before discussing results for different structures in the near wake at $Re = 1000$, it is worthwhile to comment upon their validity. The first warning concerns the numerical accuracy of the results and the resolution related to the parameters chosen. If the mesh spacing and time step become smaller and the number of grid nodes increases, the details of even finer-scale structures are better predicted. However, flow features related to more large-scale structures probably do not change considerably. In fact, computations performed for two different sets of numerical parameters gave results close to experimental ones for the mean drag and dimensionless frequency of oscillations (figure 9).

The computations discussed in the present work correspond to the set of parameters giving the best resolution possible with a reasonable CPU per time step. Consequently, these computations do not predict eddies finer than the mesh spacing chosen or unsteady phenomena faster than the scale of time step used. However, it is probable that they correctly predict larger-scale eddies of the near wake. As the present method is only second-order accurate and the mesh spacing used is $\Delta x/60$, the $Re = 1000$ results should be considered as only indicative, but they are worthy of physical analysis.

The second warning concerns the physical interpretation of results for $Re = 1000$, obtained by a two-dimensional approach. It is well known from experimental work that the three-dimensional nature of the flow at $Re = 1000$ cannot be ignored. For this reason, the ultimate goal of a complete study is to calculate all the mechanisms leading to the real three-dimensional flow: appearance of new frequencies of oscillating structures; generation of finer-scale eddies; onset of the three-dimensional motion.

The above phenomena, among others, constitute different states of the dynamics of a nonlinear system. It is worthwhile to analyse these features separately, before trying to study all of them simultaneously. A numerical approach to the problem offers the possibility of carrying out separately the above studies.

Hence, the results for $Re = 1000$ discussed in the present work are of a qualitative validity. They concern only two-dimensional properties of structures in the near wake.

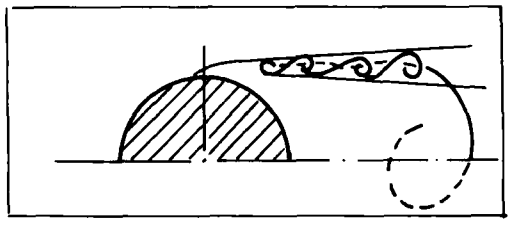

FIGURE 25. Sketch of the separated-mixing-layer eddies ($Re > 2000$).

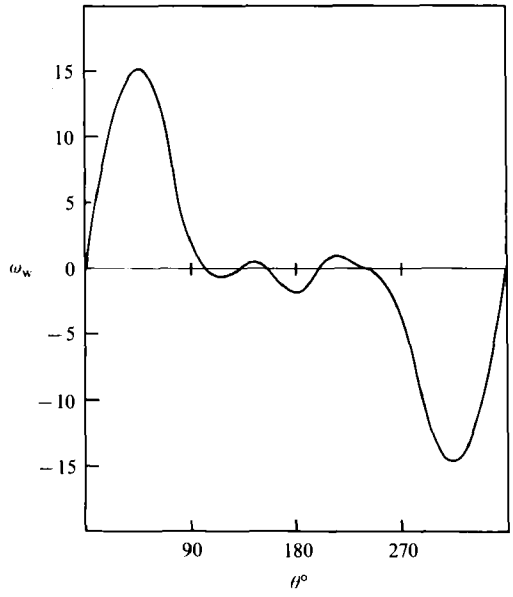

FIGURE 26. Wall vorticity at $t = 28$, $Re = 200$.

The appearance of secondary vortices is not a new property of the flow in its early stage. The experimental work of Honji & Taneda (1969) and Bouard & Coutanceau (1980) report the generation of small eddies near the wall of an impulsively started circular cylinder at Reynolds numbers greater than 300. The numerical work of Martinez (1979) and Ta Phuoc Loc (1981), based upon a vorticity–stream function formulation, study the early stage of development of such vortices, in the Reynolds-number range 300–3000. These studies are limited to short times, corresponding to the beginning of the flow.

Experimental visualizations of Crausse (1936) and Van Dyke (1982), among others, report the generation of a series of small eddies (cf. sketch of the flow pattern in figure 25), in the separated mixing layer at higher Reynolds numbers ($Re > 2000$). Furthermore, the experimental work of Roshko (1954) and Tritton (1959) locates the beginning of the laminar-to-turbulent transition at Reynolds numbers above 150–200, due to an instability that occurs in the shear layer downstream of the separation point. The problem is to identify the different kinds of structures developed in the range of Reynolds number corresponding to transition towards turbulence.

There is a lack of experimental and numerical results concerning the histories of such structures at intermediate values of Reynolds numbers (in the range 200–1000)

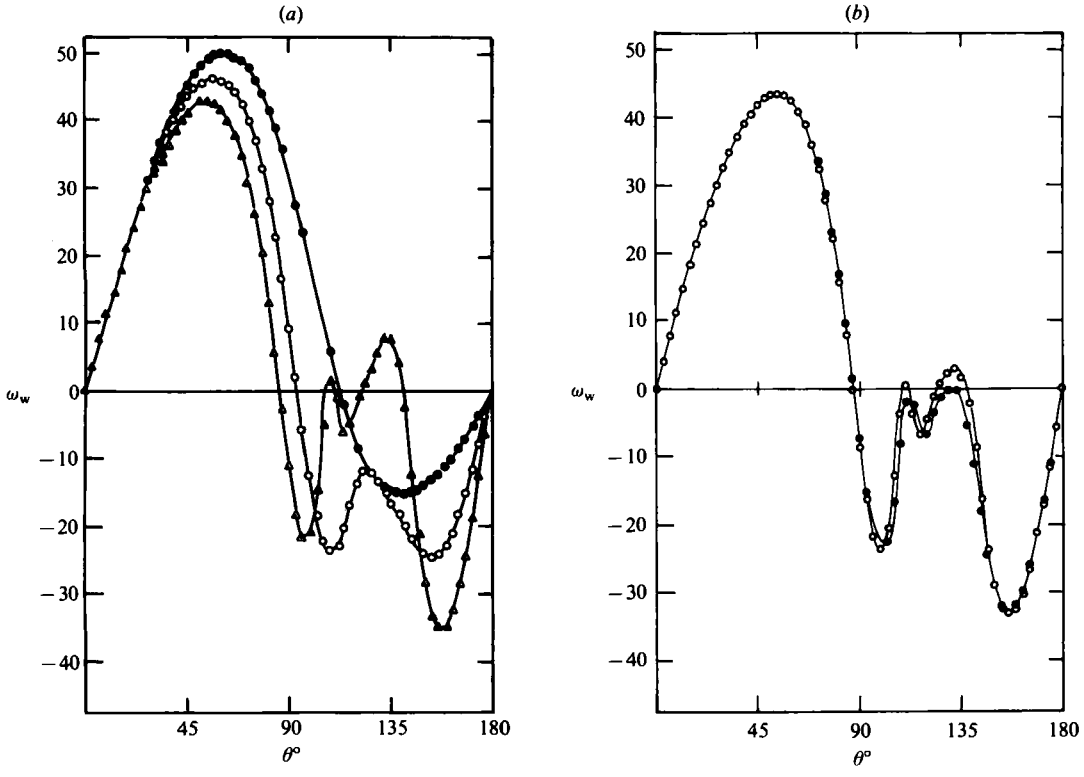

FIGURE 27. (*a*) Wall vorticity at $Re = 1000$: ●, $t = 1$; ○, 2; △, 3. (*b*) Wall vorticity at $Re = 1000$: ●, $t = 2.7$; ○, 2.8.

and over long times, as well as their influence on the development of the main vortex paths.

The present computations for Reynolds numbers in the range 200–1000 show the development of secondary eddies in the near wake, apart from the main ones of the Kármán vortex street. The Reynolds-number value of 1000 is not high enough to allow formation of the mixing-layer eddies of figure 25.

The numerical simulation developed in this paper predicts the appearance of one secondary eddy at $Re = 200$ and at dimensionless time 28 (figure 26). This secondary eddy is adjacent to the separation point, but soon disappears. This phenomenon occurs periodically up to the end of the computation ($t = 100$), at time values of 33, 39, 44, 49, 54, 59, 64, 69, 74–75, 79–80, 84–85, 90 and 95. The time interval is 5, which corresponds to a dimensionless frequency of 0.40. The energy furnished to create and sustain the secondary eddy at $Re = 200$ is not sufficient to maintain such eddies permanently. This phenomenon can be interpreted as a weak instability in the shear layer next to the separation. It is more and more pronounced as the Reynolds number increases, as described below for the $Re = 1000$ case.

First, the present simulation predicts well the early stage of development of secondary eddies at $Re = 1000$. The distribution of the wall vorticity (figures 27*a*, *b*) determines the appearance of the first secondary eddy at $t = 2.7$. Secondly, the numerical method predicts the behaviour of the secondary eddies over long times. The evolution of the secondary eddies is very different for the symmetric (non-physical)

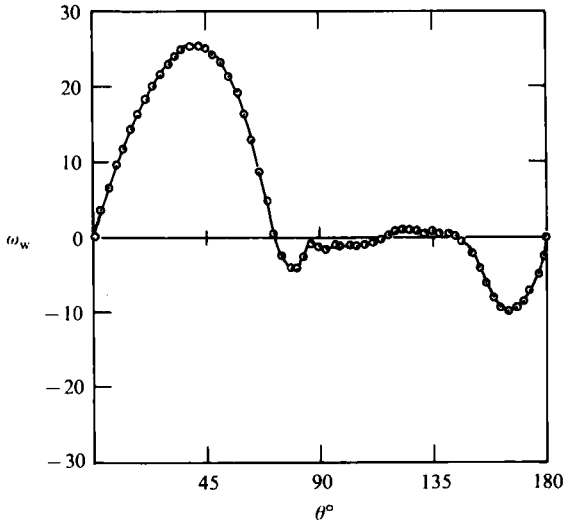

FIGURE 28. Simulation without temporary perturbation. Wall vorticity at $t = 100$, $Re = 1000$.

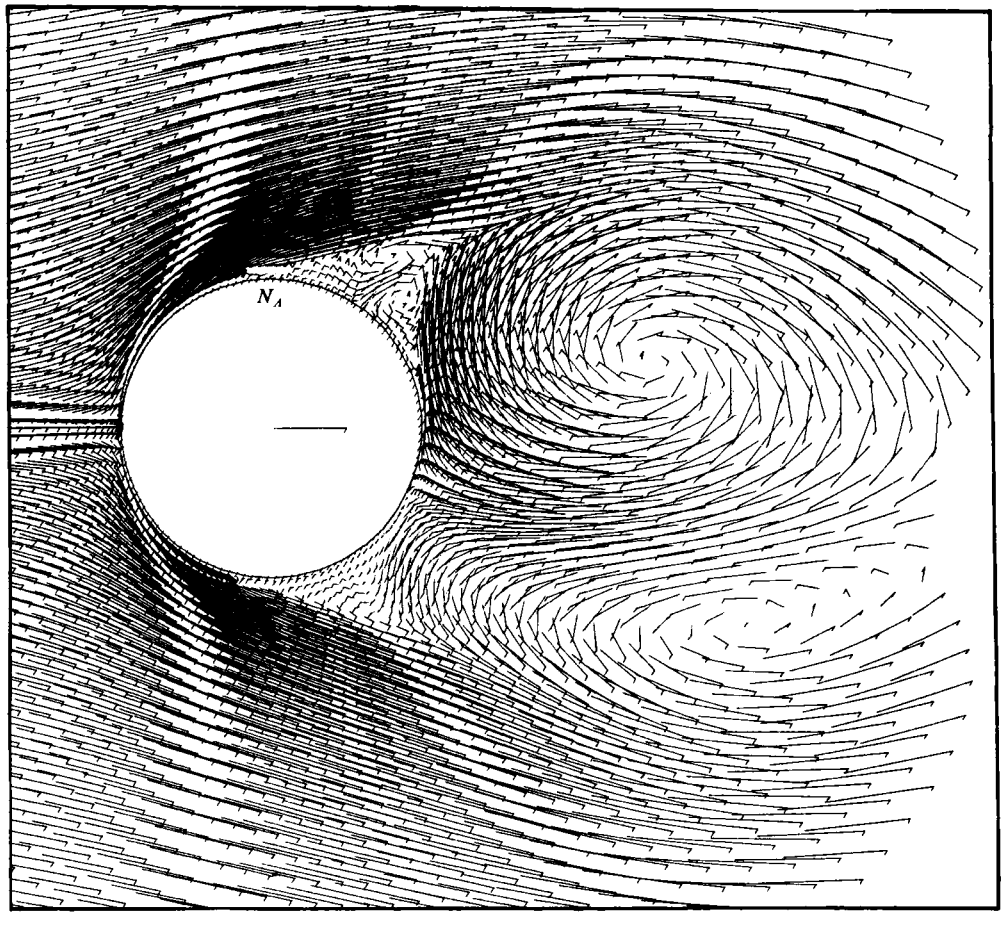

FIGURE 29. Velocity field at $t = 20$, $Re = 1000$.

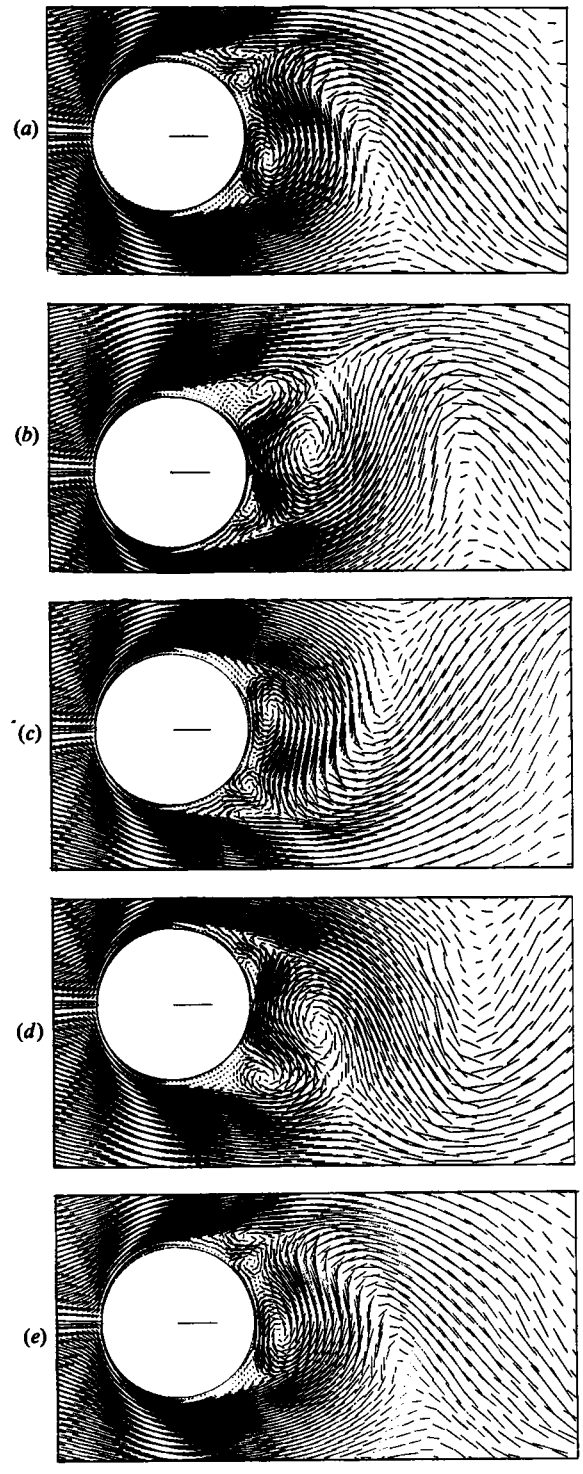

FIGURE 30. Instantaneous velocity fields at $Re = 1000$. (*a*) $t = 80$; (*b*) 82; (*c*) 84; (*d*) 87; (*e*) 89.

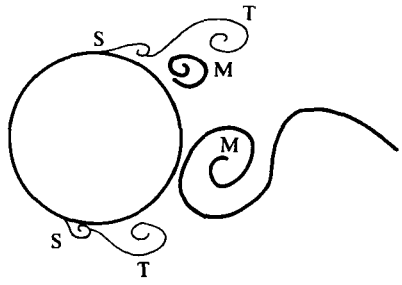

FIGURE 31. Sketch of the flow pattern with different kinds of eddies, $Re = 1000$.

flow compared with the unsteady flow with vortex shedding. In the first case the wall vorticity at $t = 100$ is symmetric relative to the rear axis (figure 28), indicating that there are two symmetric attached eddies and only one secondary eddy next to each separation point.

In the second case, two secondary vortices are formed (figure 29), followed by a smaller single vortex downstream of the separation point. This configuration agrees with the experimental and numerical results referred to above for the early stage of development of the secondary eddies. In the present study the centres of the two main vortices are not symmetric, their displacement announcing the vortex shedding. The lower main vortex has already been slightly convected downstream. The same behaviour is observed for the two corresponding secondary vortices. They have been swept by the main eddy and are not very distinct but have diffused, forming a separated bubble.

The small secondary vortex S_1 remains attached next to the separation point. The analysis of the results over a period (figure 30) shows that this property can be verified at any time. Therefore the eddies of type S_1 follow the oscillatory motion of the separation point with the fundamental frequency (figure 14).

The eddies that develop in the near wake during a given period are of three kinds (cf. the flow pattern of figures 30 and 31): the first consists of the two classic main eddies of the Kármán vortex paths (M); the second is that of the small secondary eddies (S), remaining attached and tracking the periodic motion of the separation points; the third (T) is developed in the near wake, is convected and merges with the main ones. The interactions of the eddies M and T are shown following the time-dependent evolution of velocity, vorticity and pressure fields over a period, in figure 32.

The different kinds of eddies, as well as the fluid motion, are also illustrated through streaklines formed by marker particles injected in the flow field. An overlay of streakline and of velocity-vector plots is provided for some characteristic instants in a period, for a better visualization. The dot lines on sketch figures indicate the direction of the displacement of the centres of the eddies.

The beginning and the end of the period correspond to two successive maxima of the oscillations of the lift coefficient (figure 8*d*) of the well-established vortex-shedding flow. Each characteristic value of the dimensionless time gives a phase lag from the beginning of the period, in terms of an angle $a = (t-t_1) \times 360°/(t_2-t_1)$, where t is the characteristic time value, t_1 the beginning of the period and t_2 the end.

At $t = 80$ the flow pattern of figure 32 (*a*) shows the appearance of a small secondary eddy T_2 and the development of the main eddy M_8 and of the secondary eddies T_1 and T_7. Eddy T_2 is clearly formed during $t = 80.20$ *to* 80.80. It arises from the steep velocity gradient near the wall, created by the strong rotation of fluid in eddy M_8 (see

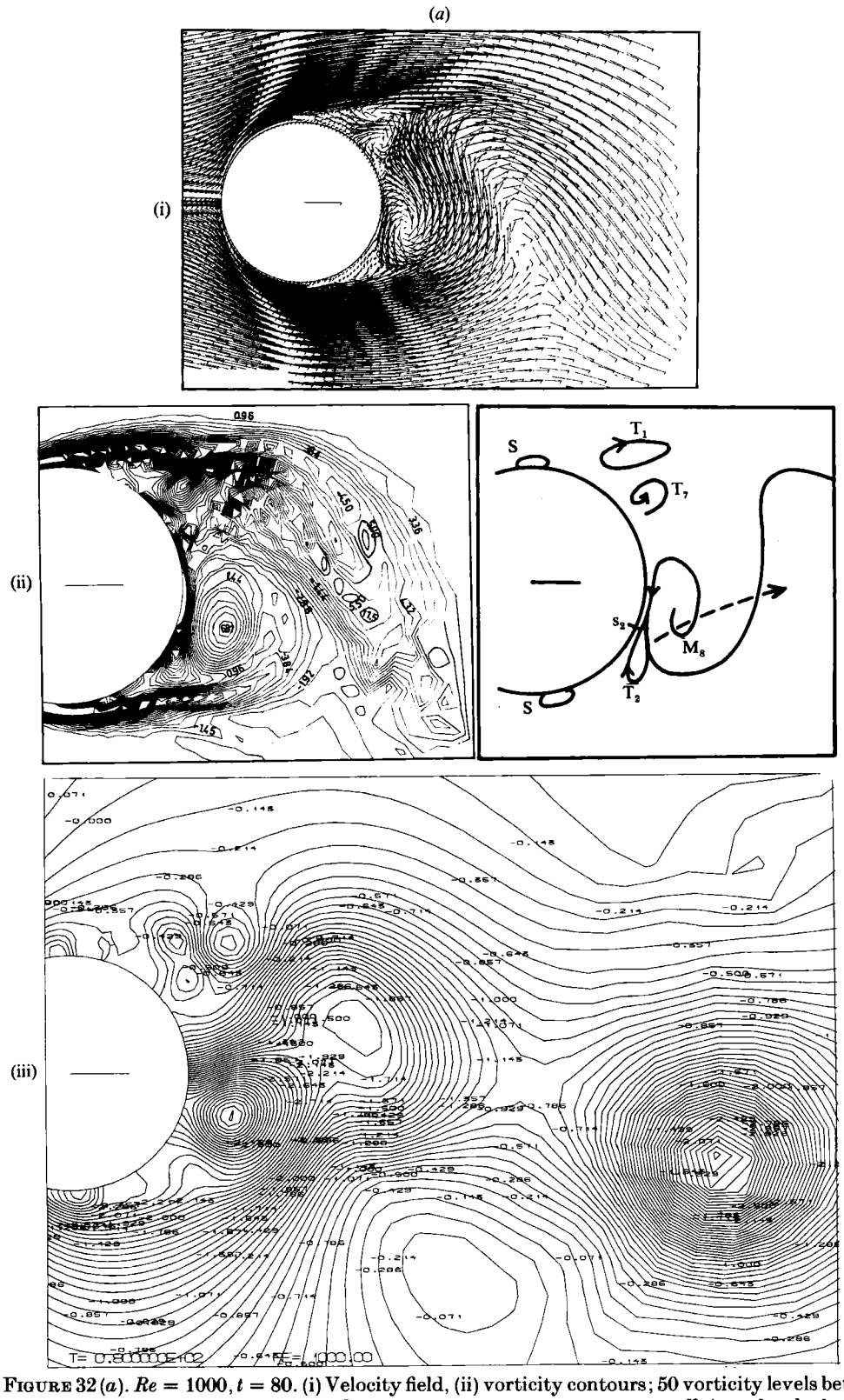

FIGURE 32 (*a*). $Re = 1000, t = 80$. (i) Velocity field, (ii) vorticity contours; 50 vorticity levels between $\omega_{\min} = -12.0$ and $\omega_{\max} = 12$. (iii) Pressure contours: 70 pressure coefficient levels between $C_{P\min} = -4.5$ and $C_{P\max} = 0.5$.

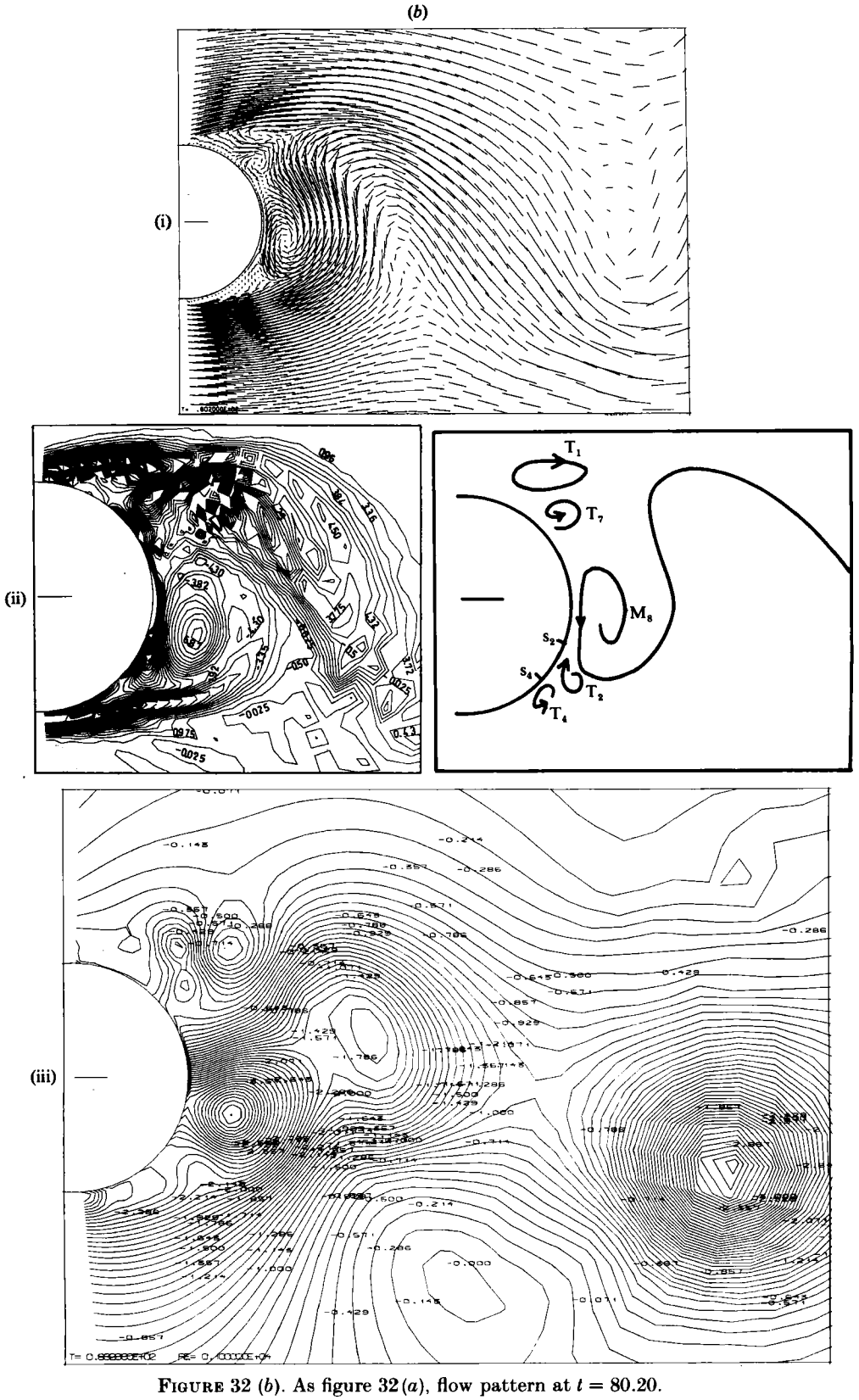

FIGURE 32 (*b*). As figure 32(*a*), flow pattern at $t = 80.20$.

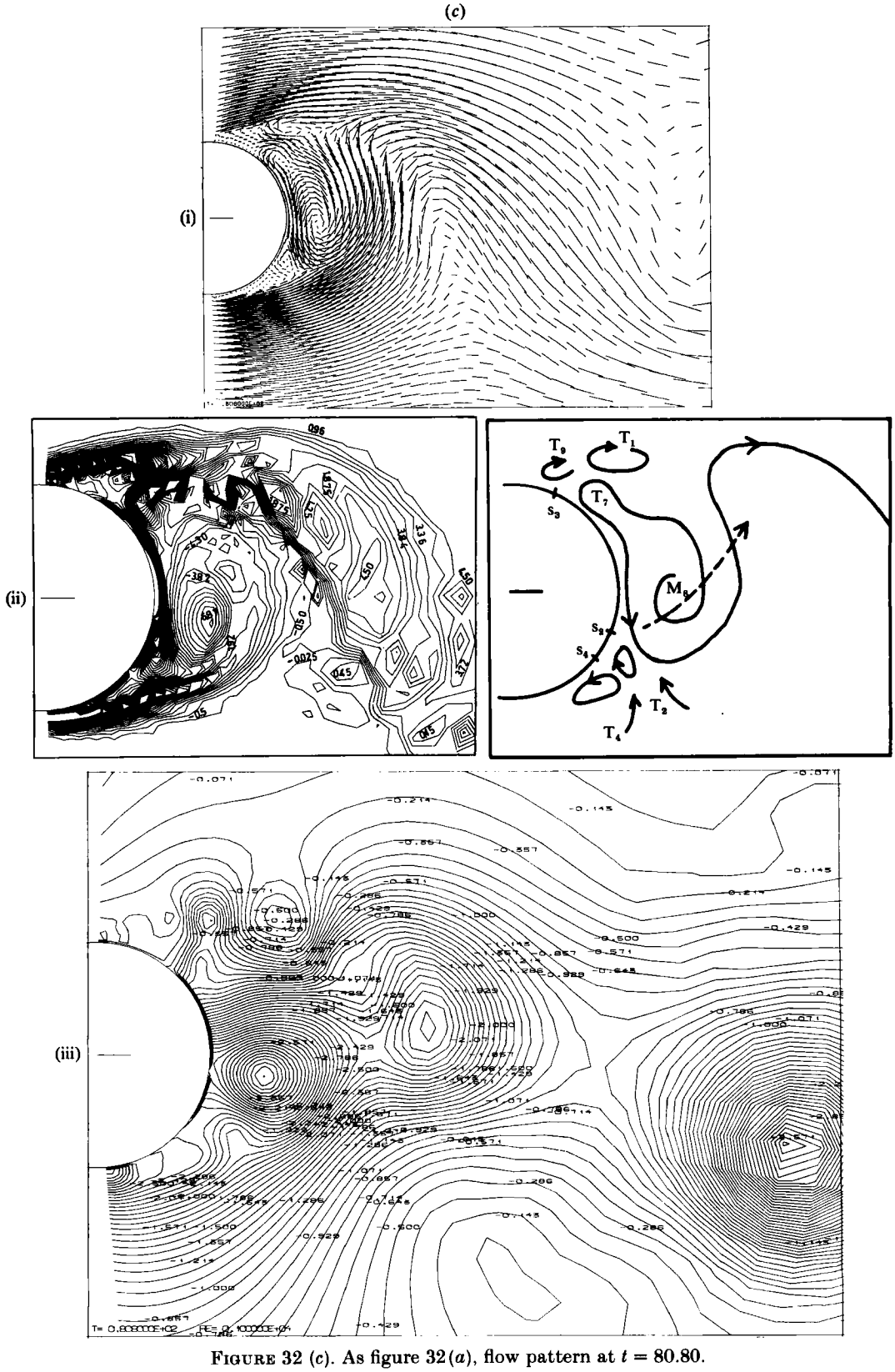

FIGURE 32 (*c*). As figure 32(*a*), flow pattern at $t = 80.80$.

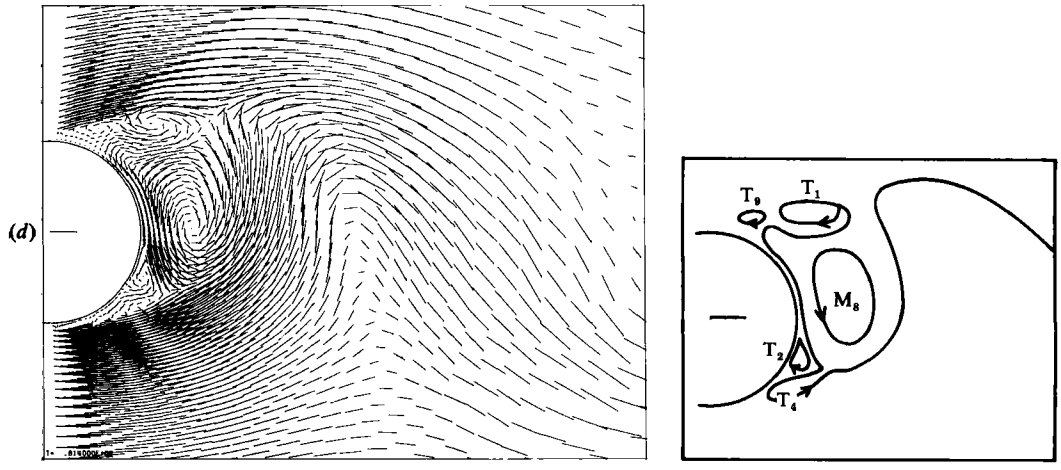

FIGURE 32 (*d*). Velocity field at $t = 81.40$.

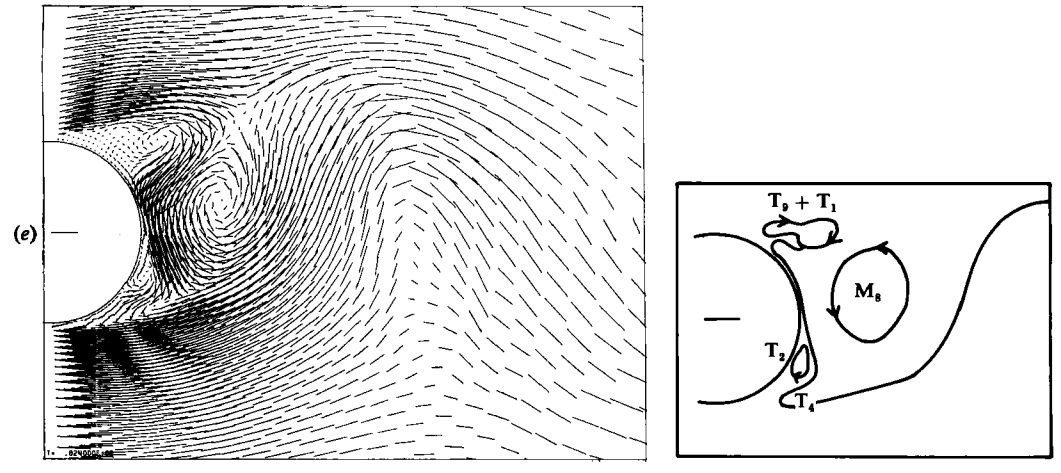

FIGURE 32 (*e*). Velocity field at $t = 82.40$.

sketch of figures 32(*b*) and 32(*c*). This is enhanced by an adverse pressure gradient towards the centre of eddy M_8, leading to engulfment of fluid from below. These factors lead to a new separation point S_2, shown also on the vorticity-contour plots.

At $t = 80.20$ a second separation S_4 occurs, owing to development of eddy T_2. This leads to formation of another eddy T_4, following the same mechanism.

At $t = 80.80$ ($a = 32°$), T_7 and M_8 merge and form one main eddy M_8 (figure 32*c*) and, simultaneously, another secondary eddy T_9 appears. The eddy T_4 has grown considerably during $t = 80$ to 80.80. This starts to merge with M_8 ($t = 81.40$, figure 32*d*), and eddy T_9 is clearly developed. The merging is achieved at $t = 82.40$ (figure 32*b*), where the beginning of merging between T_9 and T_1 is also observed.

At $t = 82.80$ (figure 32*g*) the eddy T_1 incorporates T_9 resulting in a new main eddy, M_9. The corresponding phase lag is 104°.

At $t = 84.60$, as eddy M_8 is convected downstream and eddy T_2 grows, an important velocity gradient is formed below eddy M_8 (see sketch of flow pattern figure 32*f*), leading to a new vortex T_3, clearly seen at $t = 85.0$.

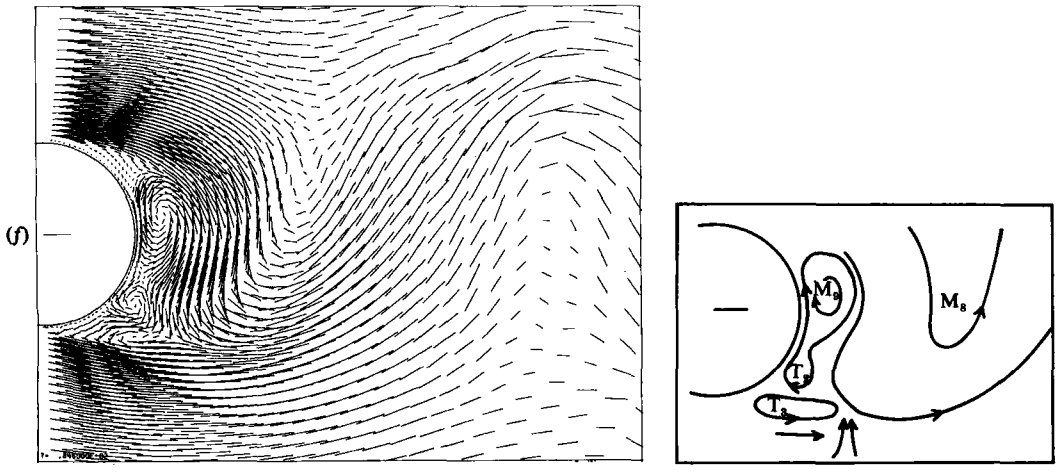

FIGURE 32 (*f*). Velocity field at $t = 84.60$.

At $t = 85$ ($a = 200°$), T_9 incorporates T_2 (figure 32*h*). Another secondary eddy also appears, similar to the well-developed eddy T_7, at $t = 80$. The same number T_7 is then used to identify this new eddy.

At $t = 85.20$ ($a = 208°$), an eddy T_{13} appears, being of the same nature as T_9. The same phenomena occur for the eddies T_{13} and T_3, as for T_9 and T_1. Another secondary eddy appears (figure 32*i*), T_{12}. This merges with the stronger main eddy M_9 at $t = 86.80$ (figures 32*i* and 32*j*). At the same time, eddies T_3 and T_{13} also merge and form a main eddy M_3.

At $t = 88.60$ (figure 32*k*) a new secondary eddy appears, of the same kind as T_1 as shown at $t = 80$. The corresponding phase difference is 344°.

The development of this eddy is due to the same mechanisms as those for eddy T_3: owing to the convection of M_9 and the growth of T_7, strong shear is created as shown in the sketch of figure 32(*k*). Also, pressure plots show engulfment of fluid in region A. These factors lead to separation of eddy T_1 from M_9.

Finally at $t = 89$ (figure 32*l*) the same flow pattern is obtained as at $t = 80$. During the next period the phenomena described above are repeated. These are summarized as follows:

Eddies of kind T are created near the wall, as a result of two different mechanisms: First, eddies like T_2, T_7, T_4 and T_{12} are due to steep velocity and adverse pressure gradients near the wall, which are a consequence of the growth of an adjacent existing eddy. These factors lead to a new separation of the flow at the wall. The above eddies grow under a diffusion effect and are found to merge later with existing, well-developed, adjacent main eddies. Secondly, eddies like T_1 and T_9, as well as T_3 and T_{13}, are formed by strong shear and engulfment of fluid in the mixing layer downstream of separation. This process does not happen near the wall. Such eddies merge (T_1 with T_9 and T_3 with T_{13}) to form main eddies.

The merging occurs under the following conditions: (i) the two eddies rotate in the same direction; (ii) one of them is convected with a higher velocity than the other; consequently the two eddies approach one another; (iii) one eddy occupies more space than the other. Each merging leads to a growth of the wake past the cylinder.

The vorticity contours shown in figure 32 illustrate clearly the formation of main eddies, and of most of the secondary ones, as defined by the corresponding velocity

(*g*)

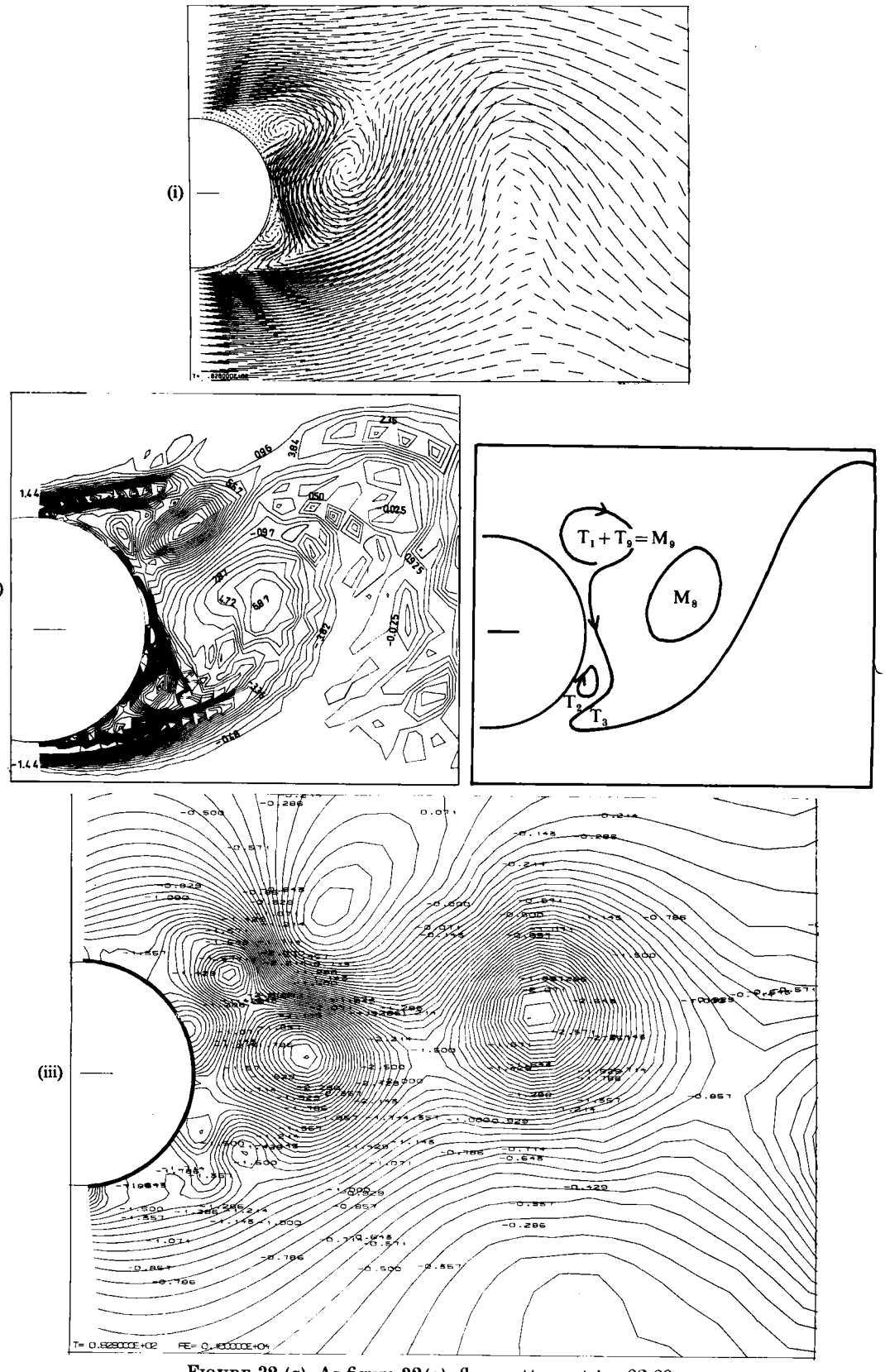

FIGURE 32 (*g*). As figure 32(*a*), flow pattern at $t = 82.80$.

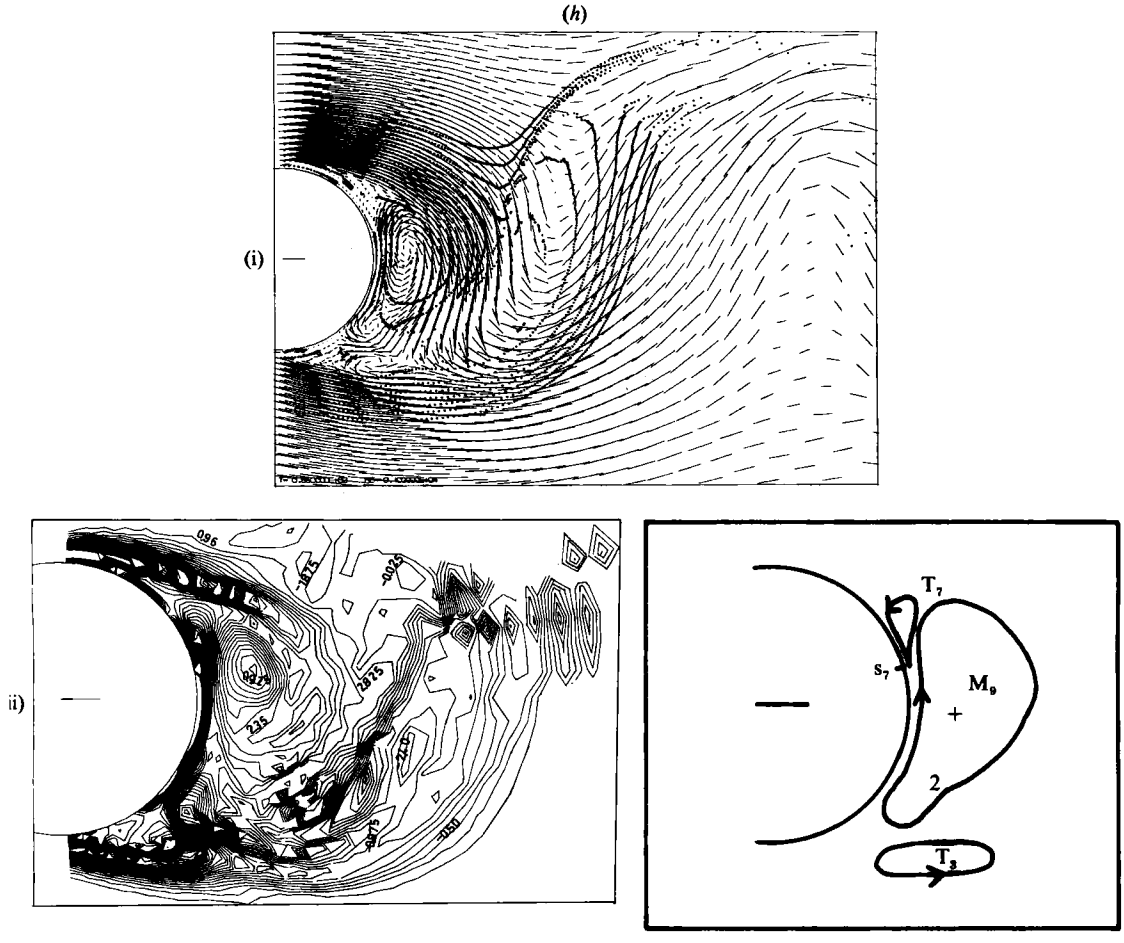

FIGURE 32 (*h*). As figure 32(*a*), flow pattern at $t = 85.00$.

fields. Vorticity peaks are located in the central area of each eddy, thus providing another means of visualization. Moreover, pressure is found to decrease towards vortex centres, as shown by pressure contours at the same time values. These features indicate rotation of fluid as a block, inside each vortex.

The above characteristics are more pronounced in regions corresponding to main eddies. In fact, these eddies are found to be more inertial than secondary ones.

The pressure variations also illustrate the different categories of eddies and they correspond to the vortex-shedding phenomenon. In fact, whenever the two main separation points are oriented counterclockwise ($t = 80.20$), the values of the upper pressure field adjacent to the separation point, are much higher than the pressure values of the lower field. The opposite behaviour occurs when the two separation points are oriented clockwise ($t = 85.0$). The pressure contours also show engulfment of fluid from regions outside the wake.

It is also found that steep pressure and vorticity gradients are developed in the separated-mixing-layer zones, which present a strongly unsteady character, delimiting a very unstable area. It is most likely that turbulence is generated from this area, rather than from alternating main-eddy regions, as Reynolds number increases.

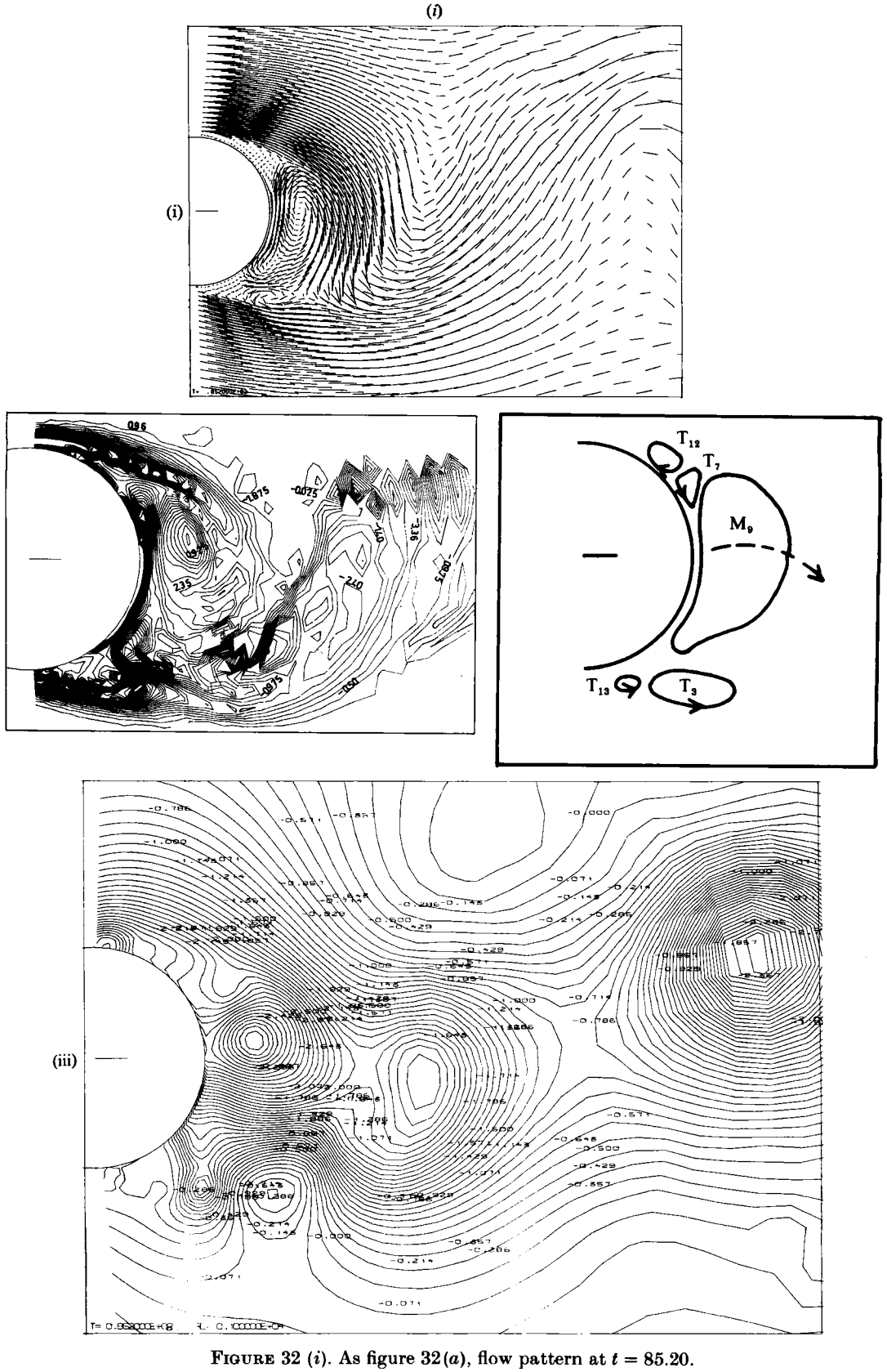

FIGURE 32 (*i*). As figure 32(*a*), flow pattern at $t = 85.20$.

(i)

(ii)

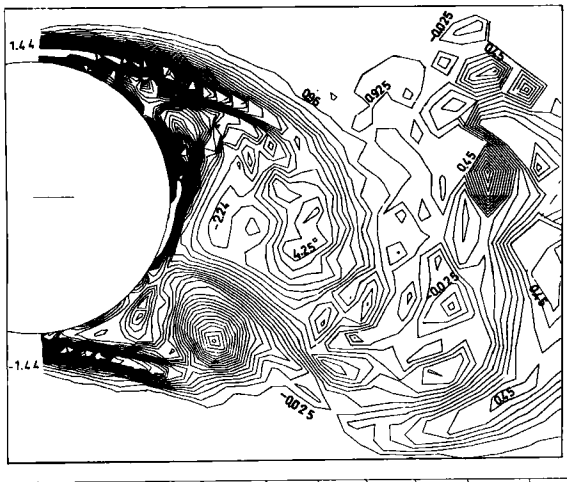

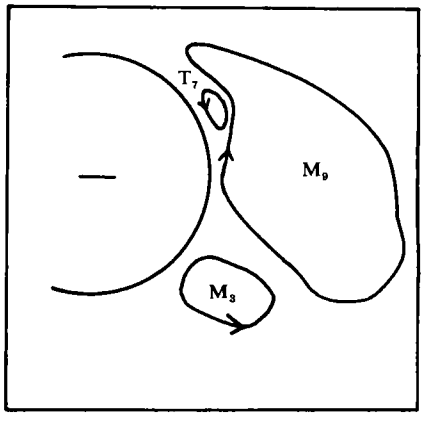

(iii)

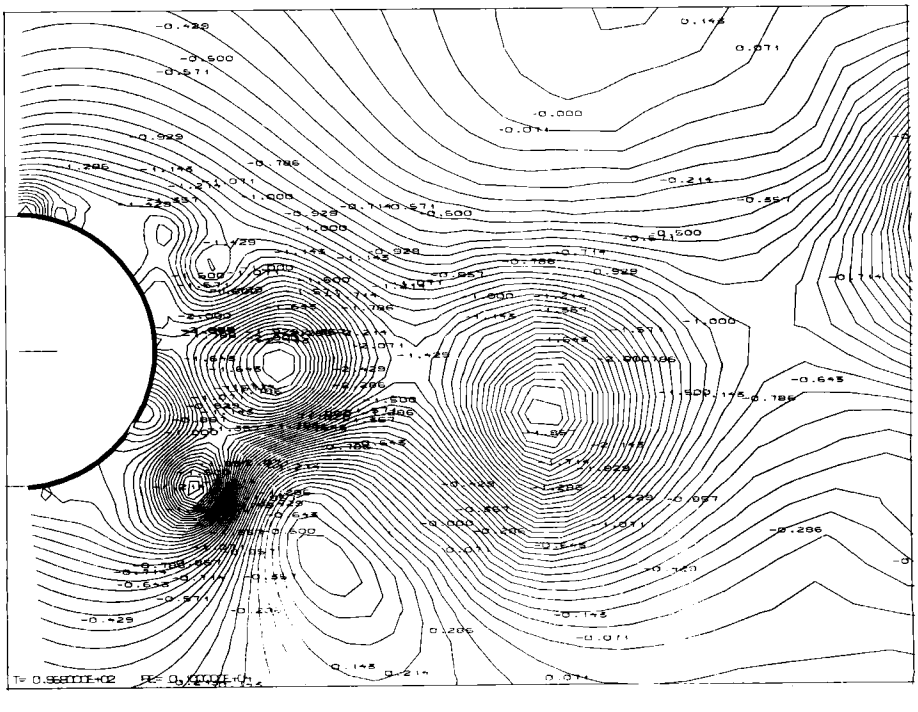

FIGURE 32 (*j*). As figure 32(*a*), flow pattern at $t = 86.80$.

(*k*)

(i)

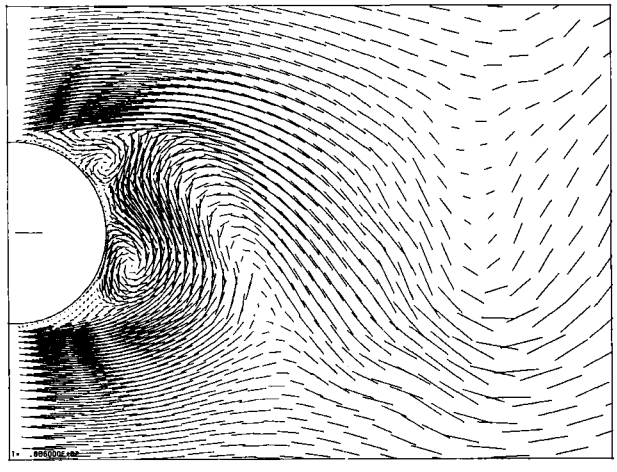

(ii)

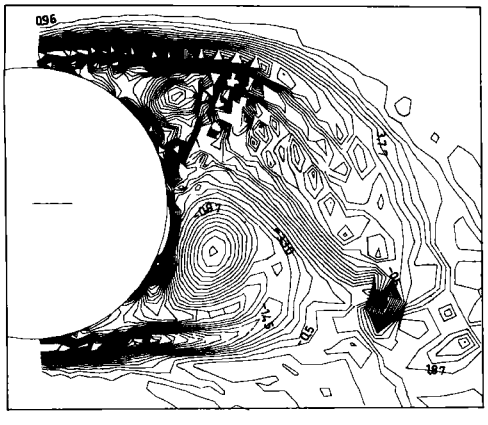

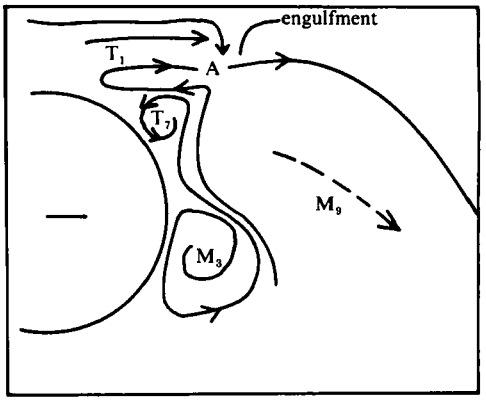

(iii)

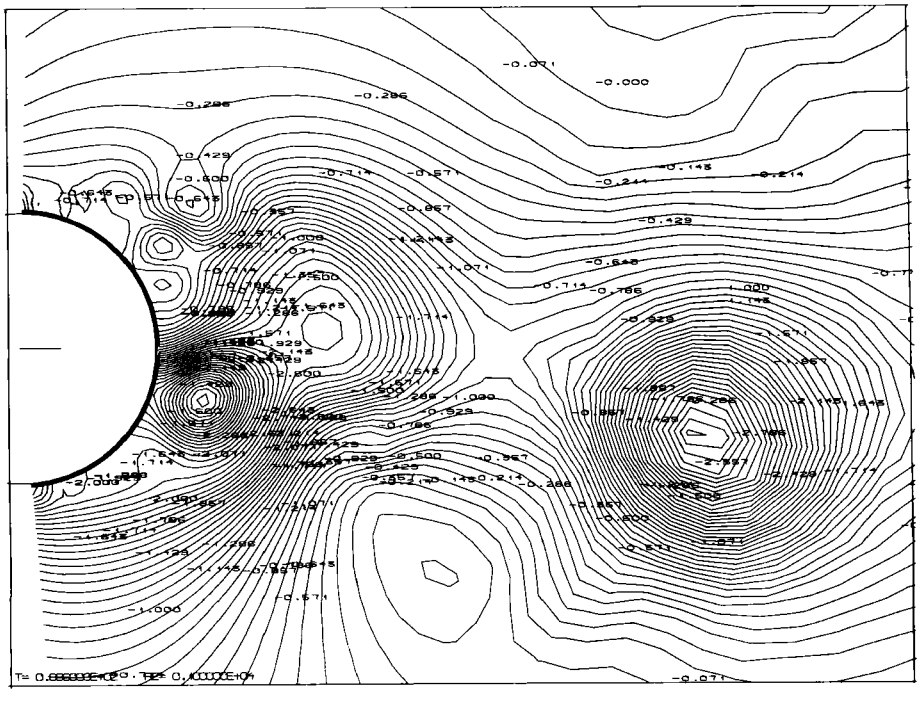

FIGURE 32 (*k*). As figure 32(*a*), flow pattern at $t = 88.60$.

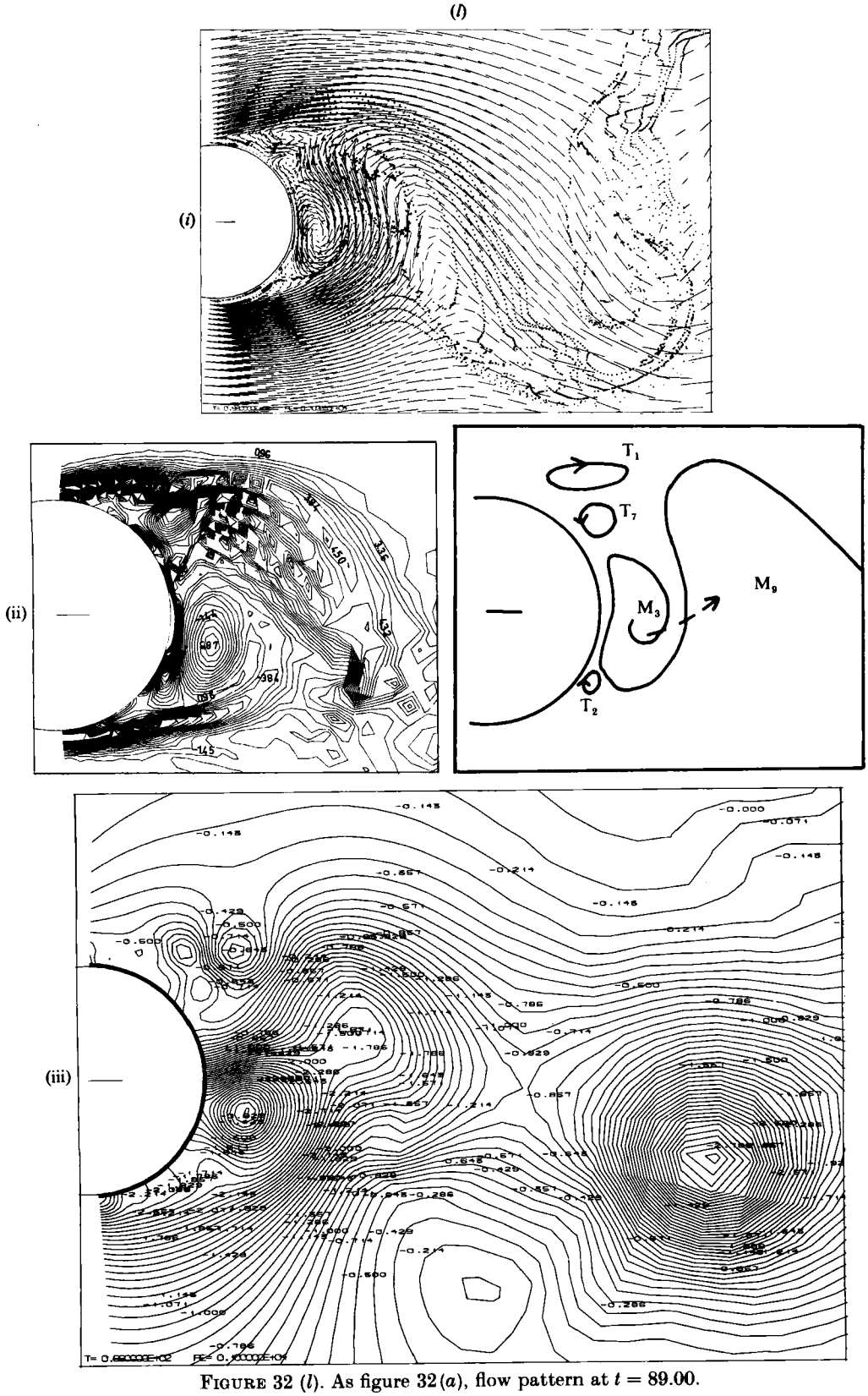

FIGURE 32 (*l*). As figure 32(*a*), flow pattern at $t = 89.00$.

The development of the secondary eddies is sustained by energy provided by the mean flow. This explains why the Strouhal number does not increase significantly beyond $Re = 200$ (figure 9*a*). As the phenomena associated with the secondary eddies appear once in a period, the global oscillatory character of the flow is preserved.

Furthermore, it is worthwhile to note that secondary eddies at $Re = 1000$ are of a different type than those appearing at higher values of Reynolds number at the end of the separated mixing layer (figure 25). The eddies of the separated mixing layer are more responsible for the laminar-to-turbulent transition than the secondary eddies discussed for $Re = 1000$. In fact, the secondary eddies at $Re = 1000$ are developed near the wall and not at the end of the mixing layer after separation. The Reynolds number of 1000 is not high enough to generate the separated-mixing-layer eddies.

Computations, not described here, using the present code in the Reynolds-number range 2000–5000 show the simultaneous development of secondary eddies and of those in the separated mixing layer demonstrating that secondary eddies are not a particular property of the $Re = 1000$ case.

As the computations are performed only in a two-dimensional configuration, the secondary instabilities developed in the near wake at $Re = 1000$ may not be exactly the same as those occurring in a physical experiment. Hence, the analysis carried out here is only a rough, qualitative description. However, these results could be used in comparisons with a physical experiment, or with other three-dimensional numerical results in a future paper, in order to understand how the turbulence appearing after separation and three-dimensional motion affect the evolution of the different structures in the wake, and also examine whether there are some features of the near-wake structures that remain two-dimensional.

5. Conclusions

The complex problem of the unsteady viscous flow around a circular cylinder is studied up to a Reynolds number of 1000 and over a long physical time. A second-order-accurate numerical method is used, based upon a velocity–pressure formulation and conservative schemes.

The first bifurcation of the Navier–Stokes equations leading to vortex shedding is well predicted by the present method. Most of the results presented in this paper are compared with experimental data and good agreement is obtained.

The study of the interactions of the unsteady pressure and velocity fields show a phase opposition of the pressure relative to the velocity at two dynamically different positions: outside and in the wake.

An analysis of different scale-structures and of their interactions during the fully developed vortex-shedding flow has shown that the secondary eddies appearing above $Re = 200$ in the near wake have a significant presence at $Re = 1000$. Pairs of them merge and form main eddies of the Kármán vortex paths, whereas another kind of secondary eddy merges with an already existing main one. All of these interactions appear once in a period. The corresponding phase lags are evaluated. The global periodic flow is not greatly influenced by these phenomena.

This work was sponsored by the Direction des Recherches Etudes et Techniques, Grant no. 83-34.061.00.470.75.01. A part of the computation time has been provided by the Centre de Calcul Vectoriel pour la Recherche. The authors are grateful to Dr H. C. Boisson for the very helpful discussions they had with him on the physical

interpretation of the results. The authors thank also Mr G. Leblanc for the computing technical assistance, and Mr J. Bonnefont, Mrs P. Herault and Mr J. Pons for their technical aid.

REFERENCES

ACRIVOS, A., SNOWDEN, D., GROVE, A. S. & PETERSEN, E. E. 1965 *J. Fluid Mech.* **21**, 737.

AMSDEN, A. A. & HARLOW, F. H. 1970 *Los Alamos Scientific Rep. No.* La-4370.

BATCHELOR, G. K. (ed.) 1960 *The Collected Works of G. I. Taylor*, vol. 2. Cambridge University Press.

BOISSON, H. C., CHASSAING, P. & HA MINH, H. 1983 *Phys. Fluids* **26**, 653.

BOUARD, R. & COUTANCEAU, M. 1980 *J. Fluid Mech.* **101**, 583.

BRAZA, M. 1981 Thèse Docteur-Ingénieur, I.N.P. Toulouse.

CAMICHEL, C. 1931 *Rapports sur les travaux effectués pendant les années* 1930 *et* 1931. Privat Editeur. Editeur.

CAZALBOU, J. B. 1983 Thèse Docteur-Ingénieur, I.N.P. Toulouse.

CHORIN, A. J. 1968 *Math. Comput.* **22**, 745.

CHORIN, A. J. 1973 *J. Fluid Mech.* **57**, 785.

COUTANCEAU, M. & BOUARD, R. 1977*a* *J. Fluid Mech.* **79**, 231.

COUTANCEAU, M. & BOUARD, R. 1977*b* *J. Fluid Mech.* **79**, 257.

CRAUSSE, E. 1936 Thèse Doctorat-ès-Sciences, Université de Toulouse.

DAUBE, O. & TA PHUOC LOC 1978 *J. Méc.* **17**, 651.

DENNIS, S. C. R. & CHANG, G.-Z. 1970 *J. Fluid Mech.* **42**, 471.

DOUGLAS, J. 1955 *J. Soc. Indust. Appl. Math.* **3**, 42.

FORNBERG, B. 1980 *J. Fluid Mech.* **98**, 819.

GROVE, A. S., SHAIR, F. H., PETERSEN, E. E. & ACRIVOS, A. 1964 *J. Fluid Mech.* **19**, 60.

HAMIELEC, A. E. & RAAL, J. D. 1969 *Phys. Fluids.* **12**, 11.

HA MINH, H., BOISSON, H. C. & MARTINEZ, G. 1980 *Trans. ASME* C: *J. Heat Transfer* **13**, 35.

HARLOW, F. H. & WELCH, J. E. 1965 *Phys. Fluids* **8**, 2182.

HONJI, H. & TANEDA, S. 1969 *J. Phys. Soc. Japan* **27**, 1668.

JAIN, P. C. & RAO, K. S. 1969 *Phys. Fluids Suppl.* (II) **12**, 57.

JORDAN, S. K. & FROMM, J. E. 1972 *Phys. Fluids* **15**, 371.

KÁRMÁN, T. VON 1911 *Phys. Z.* xiii, 49.

KOVASZNAY, L. S. G. 1949 *Proc. R. Soc. Lond.* A **198**, 174.

LILLEY, D. G. 1976 *AIAA J.* **14**, 749.

LIN, C., PEPPER, D. & LEE, S. 1976 *AIAA J.* **7**, 900.

MARTINEZ, G. 1979 Thèse Docteur-Ingénieur, I.N.P. Toulouse.

MARTINEZ, G. & HA MINH, H. 1978 In *Proc. Intl. Conf. on Numerical Methods in Laminar and Turbulent Flow, Swansea.* Pineridge.

PEACEMAN, D. W. & RACHFORD, H. H. 1955 *J. Soc. Indust. Appl. Math.* **3**, 28.

ROSHKO, A. 1953 *NACA Tech. Note. No.* 2913.

ROSHKO, A. 1954 *NACA Rep. No.* 1191.

SEARS, W. & TELIONIS, D. P. 1975 *SIAM J. Appl. Math.* **28**, 215.

SON, J. S. & HANRATTY, T. J. 1969 *J. Fluid Mech.* **35**, 369.

SPALART, P. R., LEONARD, A. & BAGANOFF, D. 1983 *NASA Tech. Mem.* 84328.

TANEDA, S. 1972 *Recent Research on Unsteady Boundary Layers*, Vol. 2 (ed. E. A. Eichelbrenner). Quebec Laval University Press.

TA PHUOC LOC 1980 *J. Fluid Mech.* **100**, 111.

TEISSIE-SOLIER, M. 1931 Thèse Doctorat-ès-Sciences, Université de Toulouse.

THOMAN, D. C. & SZEWCZYK, A. A. 1969 *Phys. Fluids, Suppl* (II) **12**, 76.

TRITTON, D. J. 1971 *J. Fluid Mech.* **45**, 203.

TRITTON, D. J. 1959 *J. Fluid Mech.* **6**, 547.
TUANN, S. Y. & OLSON, M. D. 1978 *Computers and Fluids* **6**, 219.
VAN DYKE 1982 *An Album of Fluid Motion*. Parabolic.
WACHSPRESS, E. L. 1964 *Iterative Solution of Elliptic Systems*. Prentice Hall.
WIESELSBERGER, V. C. 1921 *Physik. Z.* **22**, 321.